

DEPARTMENT OF INFORMATICS ENGINEERING
SCHOOL OF ENGINEERING
TECHNOLOGICAL EDUCATIONAL INSTITUTE OF CRETE



MSC IN INFORMATICS & MULTIMEDIA

MASTER THESIS

TEXTURE ANALYSIS ON DCE-MR AND DW-MR IMAGES

SERAFEIMIDIS IOSIF

SUPERVISOR

Dr Marias Konstantinos

COSUPERVISOR

Associate Professor Manolis Tsiknakis

HERAKLION
January 2016

Abstract

Medical Image processing and analysis aim to deliver to the clinician diagnostic and prognostic information obtained in a non-invasive way. Interpreting the content of the medical images is traditionally done by visual inspection but this reportedly leads to a high rate of false positives of malignant lesions by radiologists as well as high inter-observer variability. To tackle this problem computer-aided detection (CAD) methods have been proposed for offering more subjective, reproducible diagnostic relevant information. As an example, several CAD approaches for breast magnetic resonance imaging (MRI) have been proposed, typically either for (a) automatically detecting a lesion (computer-aided detection (CAdE)) or (b) classifying a lesion as benign or malignant (computer-aided diagnosis (CAdx)) [1]. Automated CAdE approaches usually exploit the fact that malignant lesions typically have different image intensity profile structure on MR images, compared to normal parenchyma [1].

In this thesis, the main focus was to compute several image texture measures for discriminating between benign and malignant tissue. To this end, several texture measures were implemented, including Haralick's image texture measure based on 2D image histograms [2] and fractal features [3]. The application domain concerned diffusion weighted MRI (DW-MRI) imaging which provides a measure of the random Brownian motion of water molecules within a voxel of tissue. Densely cellular tissues or those with cellular swelling exhibit lower apparent diffusion coefficients (ADC), and thus diffusion is particularly useful in tumor characterization and cerebral ischemia. Previous work on DW-MRI image processing has focused on well-known histogram-based statistical analyses which however have yielded poor results in describing tumor heterogeneity and therefore discriminating between benign and malignant masses. It has been reported that texture analysis could be a better method for achieving this [4] which led to the following research question:

Can we improve the image-based heterogeneity description and differentiate normal from cancerous tissue in DW-MRI ADC image maps by using texture analysis?

This research question has been the main rationale behind the work presented in this thesis.

Περίληψη

Η ανάλυση και επεξεργασία ιατρικών εικόνων έχει ως στόχο να παρέχει με μη επεμβατικό τρόπο στους ειδικούς διαγνωστικές και προγνωστικές πληροφορίες. Παραδοσιακά, η ερμηνεία του περιεχομένου των ιατρικών εικόνων γίνεται με οπτικό έλεγχο, αλλά υπάρχουν αναφορές ότι αυτό οδηγεί σε υψηλό ποσοστό ψευδώς θετικών διαγνώσεων κακοηθειών από ακτινολόγους, καθώς επίσης και σε υψηλή διακύμανση μεταξύ παρατηρητών. Για την αντιμετώπιση του προβλήματος αυτού έχουν προταθεί συστήματα υποβοηθούμενης διάγνωσης (CAD) τα οποία προσφέρουν πιο αντικειμενικές, επαναλήψιμες και διαγνωστικά σχετικές πληροφορίες. Ως παράδειγμα αναφέρονται κάποιες προσεγγίσεις CAD που έχουν προταθεί για εικόνες μαγνητικής τομογραφίας (MT) μαστού, με τυπικές εφαρμογές (α) την αυτόματη ανίχνευση βλαβών ή (β) την ταξινόμηση μιας βλάβης σε καλοήγη ή κακοήγη [1]. Οι διάφορες προσεγγίσεις αυτόματων CAD συνήθως εκμεταλλεύονται το γεγονός ότι οι κακοήθεις βλάβες έχουν δομικές διαφορές στα προφίλ εντάσεων απεικόνισης σε εικόνες MT συγκρινόμενα με αυτές κανονικών παρεγχυματικών ιστών [1].

Στην παρούσα εργασία εστιάζουμε στον υπολογισμό αρκετών αριθμητικών τιμών που περιγράφουν την υφή της εικόνας για την διαφοροποίηση καλοηθών και κακοηθών ιστών. Με αυτό σαν στόχο, υλοποιήθηκαν αρκετές μέθοδοι που παράγουν αριθμητικές τιμές, συμπεριλαμβανομένων και των τιμών υφής εικόνας του Haralick βασισμένων σε δισδιάστατα ιστογράμματα [2] και μορφοκλασματικά (fractal) χαρακτηριστικά [3]. Ο τομέας εφαρμογής αφορά εικόνες μαγνητικής τομογραφίας σταθμισμένης διάχυσης (MT-ΣΔ) οι οποίες παρέχουν ένα μέτρο της τυχαίας (Brownian) κίνησης μορίων νερού μέσα σε ένα χωροστοιχείο (voxel) του ιστού. Πυκνές κυτταρικές δομές ιστών ή δομές που παρουσιάζουν διόγκωση των κυττάρων παρουσιάζουν διαφοροποίηση στους συντελεστές φαινομενικής διάχυσης (ADC), οπότε η MT-ΣΔ είναι εξαιρετικά χρήσιμη στον χαρακτηρισμό καρκινωμάτων και στην αξιολόγηση εγκεφαλικών ισχαιμιών. Προηγούμενες εργασίες πάνω σε MT-ΣΔ επικεντρώθηκαν σε γνωστές μεθόδους βασισμένες σε στατιστικές αναλύσεις ιστογραμμάτων οι οποίες όμως δεν αποδίδουν καλά όταν πρέπει να περιγράψουν ετερογένεια καρκίνου καθώς και στον διαχωρισμό μεταξύ καλοηθών και κακοηθών όγκων. Έχει αναφερθεί ότι η ανάλυση υφής εικόνας μπορεί είναι καλύτερη μέθοδος για τον σκοπό αυτό [4] πράγμα που οδηγεί στην ακόλουθη ερευνητική ερώτηση:

Μπορούμε να βελτιώσουμε την περιγραφή της ετερογένειας από εικόνες και την διαφοροποίηση υγιούς και καρκινικού ιστού σε MT-ΣΔ ADC παραμετρικές εικόνες με την χρήση ανάλυσης υφής;

Η παρούσα εργασία προσπαθεί να απαντήσει στο ερώτημα αυτό.

Contents

1	Introduction.....	1
2	Literature review	3
2.1	Magnetic resonance imaging	3
2.1.1	Dynamic contrast enhanced MRI	5
2.1.2	Diffusion weighted MRI.....	5
2.2	MRI clinical applications and texture analysis.....	6
2.2.1	Brain	7
2.2.2	Prostate	8
2.2.3	Breast.....	8
2.2.4	Muscle	9
2.2.5	Bone structure.....	9
2.2.6	Kidney	10
2.2.7	Cardiovascular	11
2.2.8	Bladder	13
2.2.9	Thyroid-Neck	13
2.2.10	Liver	14
2.2.11	Pancreas	14
2.3	Texture analysis and feature extraction methods	15
2.3.1	Haralick features	16
2.3.2	Gray level difference method.....	23
2.3.3	Gradient matrix	26
2.3.4	Texture feature coding method	28
2.3.5	Run length matrix.....	31
2.3.6	Fractal features.....	33
3	Validation work	36
3.1	Dataset acquisition protocol and post processing	36
3.2	Texture analysis and feature extraction.....	38
3.2.1	Number of DWI metrics maps.....	38
3.2.2	Number of different non-ROI pixel valuessetting	38

3.2.3	Number of TA methods output maps and number of neighborhood sizes N	40
3.3	Classification and statistical analysis methods.....	42
4	Results	45
5	Discussion and Future work	47
5.1	Discussion	47
5.2	Future work	55
6	Appendix.....	57
6.1	Abbreviations	57
7	References.....	58

List of Figures

Figure 1 The GLCM of an image with 4 gray levels.	16
Figure 2 Instance of calculating the GLCM.....	17
Figure 3 There are 6 horizontal pairs of (1, 2) or (2, 1).	17
Figure 4 Instance of calculating the GLDM for horizontal pairs.....	23
Figure 5 There are 5 horizontal pairs with gray level absolute difference 2.....	23
Figure 6 Instance of calculating the GLDM for diagonal pairs (450).	23
Figure 7 There are 4 diagonal pair (450) with gray level absolute difference 0.	24
Figure 8 ROI neighborhood	26
Figure 9 Eachgroup of relative gray level of the triplets has its own code number	28
Figure 10 Each pair, regardless of order, has its own code number	29
Figure 11 The original texture (left) is converted to a 3D mesh (middle) and then enclosed in boxes of a particular size 'r' (right) thatshrinks iteratively.	34
Figure 12 Each DW-MRI is a set of slices representing a 3D volume	38
Figure 13 Each slice is rescaled to the range {0, 255}.	39
Figure 14 Copies of the ROI are made and the "nan" values are replaced by the median, mean, maximum and minimum value of the ROI.	39
Figure 15 Fromleft to right, DW-MRI slice of a pancreas ROI, its GradM map and its TFCM map	40
Figure 16 Workflow from MRI to TA feature maps.....	41
Figure 17 Algorithm for calculating the cutoff point for the classification of a single metric vector.	44
Figure 18 Kruskal-Wallis tests p-values of all the variables	45
Figure 19 AUC values of variables withnon-zero variance - 93% of total number of variables (48085 out of 51600).....	46
Figure 20 The amounts of MRI Metrics (left) and TA methods (right)that produce variableswith Kruskal-Wallis test p-values under the 0.1% and AUCs above 90%.	49
Figure 21 MRI metrics and TA methods with AUC above 90% weighted by the number of features of each TAmethod.....	50
Figure 22 Non-ROI pixel values and block sizes used to generate variables with AUC above 90%.	50
Figure 23 Neighborhood size and non-ROI pixel values in subset of variables with AUC above 90%.	51
Figure 24 Amount of features that classified the dataset perfectly with the full datasetand after the exclusion of each patient in a leave one patient out method.	52
Figure 25 MRI metrics (left) and TA methods (right) in LOPO subset.	53
Figure 26 MRI metrics and TA methods in subset 2 weighted by the number of features calculated by each TAmethod.	53
Figure 27 Neighborhood size (left) and non-ROI pixel values (right) in subset 2.....	54
Figure 28 Neighborhood size and non-ROI pixel values in the LOPO subset.....	54

List of Tables

Table 1 An example column from the table that contains all the statistical values that represent each patients' MRI.....	42
Table 2 Features with 100% AUC from the linear regression model	46

List of Equations

Equation 1 Haralick angular second moment	17
Equation 2 Haralick Contrast or inertia	18
Equation 3 Haralick Correlation	18
Equation 4 Haralick Sum of squares or variance	18
Equation 5 Haralick Inverse difference moment or local homogeneity	19
Equation 6 Haralick Sum average	19
Equation 7 Haralick Entropy	19
Equation 8 Haralick Sum entropy	20
Equation 9 Haralick Sum variance	20
Equation 10 Haralick Difference variance	20
Equation 11 Haralick Difference entropy	21
Equation 12 Haralick Information measure of correlation 1	21
Equation 13 Haralick Information measure of correlation 2	21
Equation 14 Haralick maximal correlation coefficient	21
Equation 15 logs used in Haralick's information measures of correlation and maximal correlation coefficient	22
Equation 16 GLDM mean	24
Equation 17 GLDM angular second moment or energy	25
Equation 18 GLDM Contrast or inertia	25
Equation 19 GLDM Inverse difference moment or local homogeneity	25
Equation 20 GLDM entropy	26
Equation 21 The gradient calculation for the Figure 8 ROI neighborhood	26
Equation 22 GradM mean	26
Equation 23 GradM Variance	27
Equation 24 GradM skewness	27
Equation 25 GradMKurtosis	27
Equation 26 TFCM coarseness	29
Equation 27 TFCM homogeneity	30
Equation 28 TFCM mean convergence	30
Equation 29 TFCM variance measures	30
Equation 30 TFCM code entropy	30
Equation 31 TFCM code similarity	31
Equation 32 TFCM Resolution similarity	31
Equation 33 RLM short run emphasis	31
Equation 34 RLM long run emphasis	32
Equation 35 RLM gray level non-uniformity - distribution	32
Equation 36 RLM Run length non-uniformity - distribution	32
Equation 37 RLM Run percentage	33
Equation 38 The approximation of the fractal dimension D	33

Equation 39 The counting of boxes in differential box counting.	34
Equation 40 FD of original image	34
Equation 41 High gray-value level image	35
Equation 42 Low gray-value level image.....	35
Equation 43 Smoothing an image horizontally with a window of size $2w$	35
Equation 44 Smoothing an image vertically with a window of size $2w$	36
Equation 45 Smoothing an image by averaging 4 neighboring pixels.	36

1 Introduction

Medical imaging is a generic term that refers to all the techniques that visualize body parts, tissues or organs and is a major part of modern health care as it enhances a lot of stages of the medical procedure including diagnosis, treatment, preoperative assessment and post-treatment monitoring. The main types of medical images are X-ray based methods, ultrasound and MRI and they are generally complimenting one another in providing ways to examine the human body in detail providing diagnostic information with the use of image processing techniques. Advances in electronics and computing power in the course of more than a century have made medical image processing and analysis quicker, more precise and less invasive. The present work focuses on information extraction through texture analysis on MRI images.

MRI acquisition methods produce non-invasive high-quality images of the interior of the human body that allow the visualization of soft tissues by taking advantage of the existence of water molecules combined with the use and manipulation of magnetic fields, radio waves and powerful computers. It is often the case that in order to increase diagnostic information a contrast agent (a magnetically active material) is administered to the patient in order to enhance internal structures or abnormalities. MRI is particularly good at pinpointing or assessing the growth of certain tumors, at measuring blood flow or for complementing other imaging methods. The certain advantage of MRI compared to other techniques that are also routinely used (mainly computed tomography (CT) scans, X-rays), is that it does not use radiation so it is well suited for regular use. As such, it has become a medical procedure readily available for imaging almost all organs of the human body.

The broad applicability of medical images coupled with the relative ease of acquisition has led to the need of CAD methods for quick and automatic interpretation of their content by quantitative analysis techniques. CAD methods are being continually

developed to provide radiologists with a way to fully exploit the information present in medical images by viewing the imaged object through macroscopic and microscopic level.

Expert radiologists examine MRIs and make qualitative analysis to identify parameters and other characteristics that help them detect and classify structural abnormalities on tissue. CADs examine the imaged tissue at the level of individual pixels, the smallest elements in a digital image. An **image texture** is a set of metrics calculated in image processing designed to quantify the perceived texture of an image. Image texture gives us information about the spatial arrangement of color or intensities in an image or selected region of an image¹. The pixels' grey level are usually the input of texture analysis (TA) methods and algorithms which aim to provide quantitative metrics that describe and characterize the texture of the tissues depicted [5]. TA is a quantitative method that may be sensitive enough to detect subtle changes on tissue architecture and extract more robust information comparing to simple visual inspection.

TA based on MRI is a field of research with applications in a wide variety of topics, including the detection of lesions and differentiation between pathological and healthy tissues in different organs [6] [7]. The objective of TA on MRI is to find texture (tissue) specific features that can be correlated with known pathologies and to provide information to be used alone or in combination with other clinical findings in order to allow more reliable detection and characterization or even early detection of pathologies.

In the present work we propose that TA improves the statistical classification of MRI intensity and metric maps for discriminating between benign and malignant tissue.

In chapter 2 we present a literature review on MRI imaging of several organs with emphasis on the use of TA image processing before concluding that there has been no work reported on Pancreatic MRI TA which is the clinical application domain of this

¹https://en.wikipedia.org/wiki/Image_texture

thesis. In chapter 3 we explain in detail the dataset used and analyze the proposed methodology to assess its discriminatory power for differentiating benign from malignant image regions. In chapter 4 we present the results of the proposed method on a dataset of Pancreatic MRI. In chapter 5 we discuss the results and present our intentions for further developments on the subject.

2 Literature review

2.1 Magnetic resonance imaging

MRI is a technique that produces images of a body's soft tissue without the use of ionizing radiation that is used in CT scanning or other x-ray methods. The whole process is based on the fact that water molecules are distributed differently in organs and tissues throughout the body reflecting each tissue's architectural structure. In simple and broad terms, what is depicted in an MRI scan is the position of hydrogen nuclei of the water molecules.

The hydrogen nuclei is a single proton and, like all protons, they have a property called "spin" with a given orientation and in their natural state are positively charged and their spins have randomly oriented axes so their tiny magnetic fields cancel each other out. MRI scanners utilize wire loops with electric current passing through them that produce magnetic fields with strength between 0.5 and 3 T (tesla) and the patient is laid in the space inside the loops. This will align the spin axis orientation of the hydrogen protons in the patients water molecules parallel to that of the magnetic field and some will have the same direction as the field while the rest will have the opposite direction with a slight excess in favor of the former which creates a small net magnetization of the area. Radio waves are generated by antenna coils positioned around the patient to interact with the protons and make them resonate. Those protons with the same spin axis direction as the magnetic field are in a low energy state and those in the opposite are in a high energy state. By exciting the protons with the proper radio frequency, the excess low energy protons absorb energy to become high energy protons and so their spin direction change to opposite of the magnetic field. By letting the excited protons relax,

the newly aligned protons emit the radio waves back to the antenna coils and revert to low energy and same spin direction as the magnetic field. Depending on the kind of tissue the reverting protons are in, they emit the radio waves back in different frequencies. These waves now contain encoded information in their frequency and phase that help determine each signals position and the kind of tissue they originate from [8] [9] [10].

The frequency of the radio waves used to stimulate the protons is dependent on the targeted element and the strength of the magnetic field. In the case of clinical MRI the element is usually hydrogen so the strength of the magnetic field is the only variable. By making it a gradient magnetic field, there is not one radio frequency that can excite the protons of the whole body, so targeted proton excitation is possible by keeping the gradient magnetic field constant and changing the frequency of the radio waves. In this setup, certain radio frequencies can excite the protons of certain parts of the body and this is used to pinpoint and create pictures of thin slices of the tissue where the radio frequency is just right to make the protons occupying that space resonate. The images produced are a set of tomographic depictions of slices through the patient's body. Due to the difference in magnetic properties of each type of tissue, MRI demonstrates high sensitivity in tissue variation in the form of high contrast and as such it has exceptional utility as a tool for medical diagnosis [11].

The contrast seen on MRIs is generated mainly through differences in two kinds of spin time relaxations, T1 and T2. The longitudinal relaxation time T1 is the decay constant for the recovery of the nuclear spin magnetization of the protons towards its thermal equilibrium or neutral state. The transverse relaxation time constant T2 measures the disappearance of the rotating magnetization. Depending on the weight that is given to either T1 or T2 – through the manipulation of the magnetic pulse's sequence and power and the type of tissue in the region of interest – image regions appear brighter or darker because of diverse reasons including the presence of water, fat, tumors and hemorrhages [12]. Concluding, in the last few decades MRI has become a very important device in the arsenal of diagnostic techniques of medicine. It is a painless in vivo diagnostic tool

used to produce images with high resolution and detail so they can be used to detect lesions within the body. For some procedures, contrast agents, such as gadolinium, are used to increase the accuracy of the images.

2.1.1 Dynamic contrast enhanced MRI

Dynamic contrast enhanced MRI (DCE-MRI) is an MRI acquisition technique that utilizes the rampant blood vessel growth that is part of some malignant tumors development. In normal situations, blood vessels grow up to a point where they reach a sufficient coverage of the tissue. Malignant tumors on the other hand prolong the vessel growth indefinitely. By using an intravenously paramagnetic contrast agent, such as Gadolinium [13], the acquired DCE-MRIs are baseline images prior to the contrast agent injection and multiple post-contrast images and are used to evaluate various enhancement characteristics of the lesion. The dynamic acquisition of data allows for the determination of vascular permeability. Normal tissue has a diffusion permeability characteristic that serves as a baseline. This baseline vascular permeability is compared to the vascular permeability of the tissue of interest to determine whether the tissue is non-malignant or malignant. In areas with increased blood vessel growth and increased vascular leakage, more contrast agent moves from the vascular system to the tumor tissue. The paramagnetic properties of the contrast agent increase the local magnetization, which results in stronger signal intensity depicted in the acquired image sequence. This enhancement causes the tumor area to increase in image signal intensity over time, while normal tissue areas remain at the same signal intensity, thereby making tumor tissue appear brighter than normal tissue in the image [14].

2.1.2 Diffusion weighted MRI

DW-MRI is based on the random movement of water molecules, also called Brownian motion. The properties of the movement are dependent on the environment; if the molecules are in a nonrestrictive environment they are equally diffused in all directions contrary to certain areas of the body where a diffusion directionality can be observed – isotropic and anisotropic diffusion respectively – and the viscosity of the medium or the

ease with which molecules are displaced in it, represented by a value called diffusion coefficient D [8] [15].

To quantize the diffusion, contrary to typical MRIs where only a homogenous magnetic field is used to prime the protons for the radio waves, a pulsed magnetic gradient is also applied and the resulting contrast image indicates with darker pixel intensities the areas where diffusion is stronger in the direction of the pulse. Additionally to better interpret the resulting image, the diffusion coefficient D is replaced by the apparent diffusion coefficient ADC produced by a DW-MRI and a MRI without perfusion contamination [16].

A further improvement in producing diffusion images is the use of the intravoxel incoherent motion (IVIM) model which considers the motion of the water molecules in each voxel as a combination of diffusion due to their Brownian motion, characterized by the diffusion coefficient D , and perfusion, that results from the water flowing with the blood microcirculation in the capillary network, characterized by the pseudo diffusion coefficient D^* . The number of water molecules in the voxel that flow in the capillaries is only a fraction of the total and this percent is expressed as the perfusion factor f [17].

2.2 MRI clinical applications and texture analysis

MRI plays an important role in cancer diagnosis, severity assessment, treatment planning and appraising. MRI can provide information able to help radiologists distinguish between normal and diseased tissue and to reveal cancerous tissues within the body. It is also useful for imaging metastases. MRI provides greater contrast within the soft tissues of the body and as a result, it is often used for imaging the brain, spine, muscle, connective tissue, bones marrow and other soft tissue structures and organs. In the following sections the main areas/organs of MRI application are reviewed along with relevant prior work on TA.

2.2.1 Brain

Maybe the most useful MRI of soft body tissue and with the best results currently, is in the area of the brain as it is one of the few imaging tools that can see through the skull bone and deliver high quality pictures of the brain's delicate soft tissue structures.

By comparing texture features of T2 weighted MRIs of normal appearing white matter of untreated patients versus normal white matter of healthy subjects, TA may potentially provide some prognostic evidence in relation to future disability of patients diagnosed with clinical isolated syndrome of multiple sclerosis [18].

Glioblastoma patients who have received treatment may show progression or pseudo progression of increased existing lesions or develop new ones. Contrast and correlation texture features obtained from TA of T2 weighted MRI are the most promising differential imaging biomarkers that distinguished between the two [19]. TA of ADC maps also produce texture biomarkers with pretreatment prognostic information independent of known prognostic factors like age, stage and surgical procedure [20].

In a texture segmentation effort, texture features extracted from denoised brain MRIs and subsequently introduced to a support vector machine that detects with an accuracy of 99% the tumor area and then separates the tumor region from normal brain and reconstructs it in 3D [21].

TA methods yield measurements that result in good classification between MRIs of brains with Alzheimer's disease and MRIs of normal brains and also reflect the progression of the disease. This makes TA a useful tool in the diagnosis and tracking of Alzheimer's disease [22].

Juvenile myoclonic epilepsy disease mechanisms are connected to the thalamus after investigating MRI with TA [23] and even neonatal brains, with their increased water content and structural variability due to immaturity, can be examined for ischemic injury by using techniques that have a great potential for automated injury detection from MRI data [24].

2.2.2 Prostate

In the last few decades MRI is used for diagnosis and observation of prostate cancer (CaP) and it is considered as a complementary method to the prostate-specific antigen control and transrectal ultrasound (US) biopsy, performed to distinguish low from high risk and the stage of CaP [25] [26]. MRI-ultra sound guided biopsy, where MRI is fused with US images in order to improve localization and aggressiveness assessment to carry out biopsies, has been shown to outperform standard transrectal US biopsy [27]. Gleason score is part of the evaluation of the prognosis of men with prostate cancer using samples from a prostate biopsy and there has been association identified between ADC prostate values and the Gleason score [28] [29]. Also, the detailed images coupled with the minimal invasive nature of MRI is ideal for CaP as there is generally excellent natural history reported in the series of CaP patients treated with active surveillance [30].

High resolution MRI has been shown to have a higher accuracy of prostate cancer detection compared to ultrasound and it is a natural fit for CAD systems as they provide clearer and sharper spatial information that can be interpreted into a pixel or voxel representation to be analyzed by 2-D or 3-D TA methods. Such systems, based on first and second order texture feature analysis of DCE, DW and T2 weighted MRI, have been reported to provide satisfactory results when compared with expert qualitative analysis [31] [32].

2.2.3 Breast

Breast cancer MRI is not recommended as a screening tool by itself, because although it is a test with high sensitivity, it can still miss some cancers that mammograms would detect, even for women at high risk for breast cancer [33]. It also has high false-positive findings that may lead to unnecessary biopsies or overtreatment [34]. There are some promising reports however on breast cancer quantitative classification of DCE-MRIs using volumetric TA or 4D TA (i.e. volumetric TA on pre-contrast and post contrast DCE-MRIs) with results comparable to those of radiologists [35] [36] [37].

Breast MRI may be used in addition to mammography to detect breast cancer in its earliest stage for some women who are at high risk for developing the disease [38], to better examine suspicious areas found by a mammogram, to look more closely at the breast on someone who has already been diagnosed with breast cancer [39] or to monitor for post treatment recurrence [40] [41].

2.2.4 Muscle

Whole-body MRIs (WB-MRI) is a good replacement of CT scans as a diagnostic tool in neuromuscular diseases due to limitations of the later because of the use of ionizing radiation and the artifacts from dense bone structures [42]. WB-MRI protocols like the Garchesprotocol are suitable for a large spectrum of adults and children with early-onset neuromuscular disorders [43] [44] and degenerative diseases [45]. A great advantage of WB-MRI is the correct and accurate definition of biopsy targets when a biopsy is required on patients with suspected muscle disease. Oedematous and inflammatory changed muscles can be sufficiently depicted and therefore biopsies become more precise [45] [46] [47].

Investigation of automated MRI TA of muscle ROIs, using statistical and structural methods, produce high sensitivity and specificity scores and the findings suggest that TA of MR images can provide further microscopic information complementary to the results of visual examination [48]. Muscle composition can be described with the TA of MR T2 relaxation time sequences, to help in diagnosing fat infiltration in muscular dystrophy, as fat is a marker for the progression and severity of the disease [49] [50].

2.2.5 Bone structure

Bone marrow disease diagnosis is another medical area where MRI and WB-MRI tools are becoming indispensable. Bone marrow lesion is an indication of many bone disorders that include osteoarthritis, arthritis, diffuse large B-cell lymphoma, osteonecrosis, bone bruise, multiple myeloma, and even tumor or transient bone marrow edema syndrome [51] [52] [53] [54] [55]. At least one survey has shown that diffusion weighted WB-MRI demonstrated more lesions than x-ray skeletal survey in all regions

except the skull with greater interobserver agreement [56]. In the area of bone tissue regeneration with the use of synthetic materials, a combination of micro CT and MRI shows potential for analyzing the morphology and biocompatibility of the bone implants by allowing non-invasive precise three dimensional measurements of the micro-structures and provides qualitative and quantitative analysis of bones and synthetic scaffolds [57] [58].

High resolution MRIs (HR-MRI) techniques are proposed to quantify and characterize bone trabeculation that causes osteoporosis. Fractal geometry has been used to quantify the convolutedness of the marrow-trabecular bone interface in the places where their existence in the bone is greatest according to image thresholding techniques [59]. Additional studies combined texture metrics of MRIs with bone mineral density measurements in a multivariate-regression model that significantly improved the analysis of bone strength and quality [60]. The usefulness of trabecular bone structure parameters assessed with TA of HR-MRI has been further compared with those determined in specimen sections and significant correlations have been found albeit with some limitations with thinner sections [61].

Significant differences are also found in the trabecular bone texture, particularly at the superior femoral neck, between people with different physical exercise loading. The differences in the femoral neck area of the bones in two groups, one of female athletes and a nonathletic reference group, were detected and classified quantitatively by MRI TA methods, specifically co-occurrence matrix-based texture parameters [62].

2.2.6 Kidney

DW-MRI of the kidney seems to be a reliable way to differentiate normal renal parenchyma and different renal diseases [63]. It has been shown that MRI is better than CT scans for evaluating malignancy, for preoperative assessment of renal lesions with minimal amounts of fat or with intracellular fat, for examining complicated cysts and it is an excellent method of preoperative workup on donors [64]. The use of kidney MRI

T2-star method for evaluating renal iron overload in thalassemic patients has also shown better results than the application of the same method on heart or liver [65].

Until a few years ago, not much progress had been made in automatic image analysis methods through TA on renal MRI because of the large amount of time and skill required for image co-registration and segmentation, so they often got ignored in renal studies and even in clinical research [66]. Some efforts have been made recently to reduce motion artifacts, due to respiratory motion, in image time series and improve the automatic segmentation of renal DCE-MRI data, concluding in results that are in agreement with manual delineations [67] [68]. Progress has been also made in image grading of renal cell carcinoma tissue through 3D TA using GLCM and Haar wavelets, with the second providing better classification accuracy [69]. Still, the quantification of MR renography is in need of improvement in all areas, but especially in the tools for automatic image analysis because of the decrease of signal-to-noise ratio with decreasing kidney function [70] [71].

2.2.7 Cardiovascular

Cardiac MRI (CMRI) has become a common test used to diagnose many diseases and conditions of the heart and major blood vessels. Cardiomyopathy encompasses a wide range of fairly rare myocardium pathologies that differ from each other in a number of ways and CMRI is considered the most important imaging technique required to differentiate, diagnose and study them [72]. DCE-MRI appears to be viable for non-invasive and pre-interventional assessment of the status of the coronary sinus in heart failure patients [73] and for detecting scarring of the damaged myocardium caused by myocardial infarction [74], which in turn can identify patients with predisposition to ventricular arrhythmias [75].

For cardiac tumors CMRI is the most useful among the available imaging modalities, as it differentiates tumor from thrombus, distinguishes benign from malignant masses, helps to determine the extent of the invasion in the myocardium and pericardium and it is used to guide surgical planning, like tumor resectability [76] [77].

Cardiac fibrosis, referring to the heart valves, can be observed by the differences on segment-based myocardial T1 maps between relaxation times in aortic regurgitation and in normal hearts [78]. The diagnosis and treatment of congenital heart disease by cardiac catheterization is based on real time observation and guidance of the catheter and the techniques employed to do that are fluoroscopy and MRI. While the former has drawbacks, like poor soft tissue visualization and exposure to radiation, the latter is safer with lower radiation exposure and better soft tissue visualization [79]. Even in newborns afflicted with congenital heart disease, MRI can help valuate cerebral hemodynamics, metabolism and risk indicators of brain injury [80].

The diagnosis and assessment of cardiovascular shunts (deviations from the normal circulatory system), is greatly benefited from CMRI as it can identify and characterize defects in the ventricular septum, quantify shunts and their impact on cardiac function, and help in the procedures of percutaneous device placement [81]. Therapy strategies of pericardial diseases, like inflammation and constriction, benefit from the morphologic and functional information that CMRI can provide by identifying and outlining the spread of pericardial masses [82].

Tagged CMRI is a technique that makes it possible to measure anatomical and functional myocardial parameters in vivo by creating temporary features - tags on an initial CMRI to create a grid of tags and then analyze the deformities of the grid through a series of subsequent CMRI depicting the tissue from different angles [83] [84]. TA, active contours, template matching and active geometry are also integrated with tagged CMRI to enable an automatic detection of the myocardial boundaries and then an optimized tracking of the grid of tags within the myocardium [85] [86]. While these methods provide good results they suffer from long processing times [87], a shortcoming not present in the harmonic phase (HARP) algorithm which works in k-space, i.e. the Fourier domain and it's a method widely accepted by the medical community as a standard processing technique for tagged CMRI [88] [89].

Texture and image analysis techniques are also used on untagged CMRI to segment the heart and blood vessels for 3D visualization using two-phase active contours [90], to

segment and investigate morphology and function of the left and right ventricular on 4-D CMRIs [91] and to retrieve CMRIs from databases based on texture indexing [92].

2.2.8 Bladder

DW-MRI is a moderately accurate technique for the local staging of bladder cancer but the accuracy for differentiating superficial versus invasive and organ-confined versus non-organ-confined tumor is high [93] [94] [95] [96] and it is also beneficial to use on patients for better preoperative T staging [97]. As bladder cancer demonstrates angiogenic activity, contrast patterns in DCE-MRI are also valuable indicators for tumor profiling [98].

TA has shown some promise in differentiating between bladder cancer and the bladder wall on MRI [99]. Bladder cancer has significant differences in some texture features compared to normal wall tissue. Some properties of bladder cancer, such as the depth of invasion into the bladder wall and surrounding structure, and the fully 3D structure of the cancer, might be obtained directly from a patient's MRI [100].

2.2.9 Thyroid-Neck

For thyroid cancer, sonography has the advantage over MRI because it is inexpensive and provides more information on tumors and metastases in the area [101] [102] but when the tumor extends to the thyroid margin DW-MRI can be used effectively and when coupled with CT can be also used to diagnose and monitor swellings, as well as perform pre-surgical imaging and evaluate for recurrence in the post-treatment neck [103] [101] [104].

A study has shown that MRI TA proves useful in correctly classifying oropharyngeal squamous cell carcinoma according to the status of p53, which is a protein that regulates gene expression to prevent cancer formation. Several texture variables were found significant enough to be used in a predictive model with 80% accuracy [105].

2.2.10 Liver

DCE-MRI is considered the state of the art method for early detection of liver tumors, as some cases can benefit from curative liver resection in early stages [106]. Also the observation and quantification of liver DW-MRI parameters seems very promising since it may help to evaluate tumor microvascularization in relation to disease progression and to assess early response to antiangiogenic treatment [107]. Liver diagnosis greatly benefits from the principle of intra-voxel incoherent motion MRI (IVIM-MRI) as perfusion fraction f and perfusion-related diffusion coefficient D^* are strongly associated with the difference between normal livers versus fibrotic livers and livers with hepatocellular carcinoma [108] [109] [110].

It has been shown that MRI TA can be used to successfully separate cirrhotic patients and healthy volunteers [111]. Performed on rats liver samples produced good results when used to classify protective or therapeutic effects of antifibrotic drugs. Liver function tests and histopathological analysis on the same samples resulted in comparable outcomes as those found by the texture parameters used in the analysis [112]. Another study on hepatic fibrosis found that the results of the TA method of finite difference and an artificial neural network reflect the degree of fibrosis most accurately [113].

2.2.11 Pancreas

Pancreatic cancer (PaC) is one of the most lethal forms of cancer as it is progressing aggressively, there is an inadequacy of tools for early diagnosis and there is no real progress in the establishment of new therapeutic options in the last two decades [114]. Due to the lack of early symptoms and the tendency of PaC to invade adjacent structures or to metastasize at an early stage, many patients with pancreatic cancer already have advanced disease at the time of their diagnosis and therefore they exhibit a high mortality rate [115]. The first diagnostic tool used is usually US followed by CT for pre-operative examination in patients with suspected PaC but currently MRI with magnetic resonance cholangiopancreatography is considered superior in several specific

situations (i.e. small tumors, hypertrophied pancreatic head, isoattenuating PaC, and focal fatty infiltration of the parenchyma [116]) given its greater soft-tissue contrast of MRI compared to that of CT [117].

Based on our extensive search, there doesn't seem to be any published research on the subject of TA on pancreatic MRI. For this reason in this thesis it was decided to investigate the use of TA for discriminating between benign and malignant masses on a dataset of pancreatic MRIs.

2.3 Texture analysis and feature extraction methods

Texture has no formal definition in the literature though it has been described as a pattern of variations in gray tones [118] [5], as a scale depended spatial relationship between tonal primitives (pixels) [2] or that it expresses if an image characteristics are fine or coarse, smooth or irregular, homogeneous or inhomogeneous [119]. Humans use mainly texture and color to differentiate materials on sight because even though texture, like shape, is a spatial property, it only reveals itself as such under very close scrutiny as it blends with and changes color to give materials the various characteristics that the human eye is trained to recognize [120]. The textures depicted on digital images are treated with a procedure known by the generic name texture analysis and it is used to extract features that describe the textures directly or in an abstract way. Apart from the obvious advantage of speed in automatic bulk digital texture processing, a big benefit over human eye perception is that the human eye can identify only first or second level complexity information from an image rather than the higher level of information a digital texture process can extract [5].

The main TA methods are the statistical, the structural and the model based methods [121]. These methods create a pool of features that are then used to classify the texture by using one of a multitude of statistical classification techniques. Which technique will be used depends on a number of things. The existence or not of a training set will lead to a supervised or unsupervised classification respectively. The number of available features is also an important factor as a high-dimensional space is difficult to be

visualized and is computationally heavy. Usually in TA of medical images samples of known pathologies a supervised classification method is used because the results have to be comparable to the known cases of pathologies to determine the usefulness of the extracted information.

2.3.1 Haralick features

The Haralick features have become a staple of medical imaging TA since Haralick et al. described them in [2]. They are second order statistics information that are extracted from a matrix representation of the relationship between pairs of pixels which must be in grayscale or at least have their color values quantized in some similar fashion. In the original publication by Haralick et al. the matrix was named gray-tone spatial-dependence matrix but now it is referred to as grayscale co-occurrence matrix (GLCM) in the literature. The GLCM contains non-normalized frequencies that are the counts of appearance of every possible pair of intensity values (usually gray scales) between two pixels separated by a distance d and orientation θ . In its most typical form the GLCM is calculated using distance d equal to 1 pixel – so neighboring pixels form the pairs – and for the orientation θ one of the 0° , 45° , 90° or 135° degrees. The occurrences of intensity pairs are stored in the GLCM according to a template grid created by all the possible pairs of intensities which is an $N \times N$ matrix, where N is the maximum intensity value possible for a given ROI.

		Intensities			
		1	2	3	4
Intensities	1	(1,1)	(2,1)	(3,1)	(4,1)
	2	(1,2)	(2,2)	(3,2)	(4,2)
	3	(1,3)	(2,3)	(3,3)	(4,3)
	4	(1,4)	(2,4)	(3,4)	(4,4)

Figure 1 The GLCM of an image with 4 gray levels.

In Figure 2 we see a step in the process of creating a GLCM of a ROI with distance 1 and orientation 0° . The black numeric values are the intensities of the ROI which, if it is

necessary, is quantized in a positive integer scale in preprocess. The arrows show an example of pair counting, in this instant it is that of the pixels with intensity 1 and 2. The count is then stored in the GLCM as shown in Figure 3.

NaN	1	1	2	2	1	NaN
3	1	2	4	3	1	
1	4	4	2	NaN		
4	1	2	4	2	NaN	
NaN	5	1	2	6	1	NaN

Figure 2 Instance of calculating the GLCM.

		Intensities			
		1	2	3	4
Intensities	1	0	6	1	1
	2	6	0	0	4
	3	1	0	0	1
	4	1	4	1	2

Figure 3 There are 6 horizontal pairs of (1, 2) or (2, 1).

After the creation of the GLCM comes the feature extraction process which provides quantitative features for analysis the texture content of the image. Haralick et al. proposed 14 features which are described in the following sections.

2.3.1.1 Angular second moment

Angular second moment (ASM) or energy that measures the smoothness of the image and it is calculated from the sum of the squares of the entries of the GLCM. If an image is smooth ASM is large because the values of GLCM are less uniformly distributed and there are a few large frequencies present. If the image is not smooth then the GLCM is populated by a lot of small values and the ASM is small.

$$f_1 = \sum_i \sum_j \{p(i,j)\}^2$$

Equation 1 Haralick angular second moment

2.3.1.2 Contrast

Contrast or inertia is a measure of local level variation. Visually the GLCM is fuller and with higher frequency values at the corners away from the main diagonal where the pairs of pixels with large intensity difference are situated. It is calculated by summing all the frequencies of the GLCM after weighting them in favor of the pairs with higher intensity difference.

$$f_2 = \sum_{i=0}^{N_g-1} n^2 \left\{ \sum_{i=1}^{N_g} \sum_{j=1}^{N_g} p(i, j) \right\} \\ |i - j| = n$$

Equation 2 Haralick Contrast or inertia

2.3.1.3 Correlation

Correlation is the measure of linear dependency between each pair of pixels represented in the GLCM. The more pairs found with similar grayscale intensities the higher the correlation measure.

$$f_3 = \frac{\sum_i \sum_j (ij) p(i, j) - \mu_x \mu_y}{\sigma_x \sigma_y}$$

Equation 3 Haralick Correlation

2.3.1.4 Sum of squares

Sum of squares or variance is a measurement of the spread between the intensity pairs in the image. It is the mean of the product of the differences of all the intensity pairs from their marginal means.

$$f_4 = \sum_i \sum_j (i - \mu)^2 p(i, j)$$

Equation 4 Haralick Sum of squares or variance

2.3.1.5 Inverse difference moment

Inverse difference moment or local homogeneity is a measure inversely proportional to the contrast of the image. Images with small local intensity variations have a large amount of local homogeneity.

$$f_5 = \sum_i \sum_j \frac{1}{1 + (i - j)^2} p(i, j)$$

Equation 5 Haralick Inverse difference moment or local homogeneity

2.3.1.6 Sum average

Sum average is calculated by first adding the intensities of each possible intensity pair in the GLCM and then summing the frequency of the pairs with the same total intensity. This produces an array of length $2N-1$ (where N the maximum intensity value). Another way to get the same result is to sum all the elements of each of the secondary diagonals of the GLCM. The sum of the products of each element of the array times the corresponding total pair intensity of the element gives the measure of the sum average.

$$f_6 = \sum_{i=2}^{2N_g} i p_{x+y}(i)$$

Equation 6 Haralick Sum average

2.3.1.7 Entropy

Entropy is a measure of how evenly energy is distributed and is related to the contrast of the image. The smoother the image the lowest the entropy value. For the GLCM calculating the entropy means quantifying the repetition of intensity pairs and thus measuring the repetition of the texture. Low entropy means more repetition and higher entropy means more randomness in the structure of the texture.

$$f_7 = \sum_i \sum_j p(i, j) \log(p(i, j))$$

Equation 7 Haralick Entropy

2.3.1.8 Sum entropy

Sum entropy is the entropy of the array calculated by adding the intensities of each possible intensity pair in the GLCM and then summing the frequency of the pairs with the same total intensity, as in sum average described above.

$$f_8 = - \sum_{i=2}^{2N_g} p_{x+y}(i) \log\{p_{x+y}(i)\}$$

Equation 8 Haralick Sum entropy

2.3.1.9 Sum variance

Sum variance is the same as sum average but with total intensity pair array being replaced by the squared difference of the sum entropy measure from the total pair intensity.

$$f_9 = \sum_{i=2}^{2N_g} (i - f_8)^2 p_{x+y}(i)$$

Equation 9 Haralick Sum variance

2.3.1.10 Difference variance

Difference variance is calculated by first subtracting the intensities of each possible intensity pair in the GLCM and then summing the frequency of the pairs with the same difference in intensity. This produces an array of length N (where N the maximum intensity value). Another way to get the same result is to sum all the elements of the diagonals of the upper triangle of the GLCM multiply them by 2 and then add to the array the matrix trace. Then the variance of this array is calculated to produce the measure of difference variance.

$$f_{10} = \text{variance of } p_{x-y}$$

Equation 10 Haralick Difference variance

2.3.1.11 Difference entropy

Difference entropy is calculated as the normal entropy above but with the values of the GLCM that have the same difference in gray levels added. The smoother the image the lowest the entropy value. For the GLCM calculating the entropy means quantifying the repetition of same difference intensity pairs and thus measuring the repetition of relative gray level values in the texture. Low entropy means more repetition and higher entropy means more randomness in the structure of the texture.

$$f_{11} = \sum_{i=0}^{N_{g-1}} p_{x-y}(i) \log\{p_{x-y}(i)\}$$

Equation 11 Haralick Difference entropy

2.3.1.12 Information measures of correlation and maximal correlation

Information measures of correlation and the maximal correlation coefficient are introduced in [122] and [123] and according to [2] provide some desirable properties that are not available from the simple correlation calculated above.

$$f_{12} = \frac{HXY - HXY1}{\max\{HX, HY\}}$$

Equation 12 Haralick Information measure of correlation 1

$$f_{13} = (1 - \exp[-2(HXY2 - HXY)])^{1/2}$$

Equation 13 Haralick Information measure of correlation 2

$$f_{14} = (\text{Second largest eigenvalue of } Q)^{1/2}$$

Where

$$Q(i, j) = \sum_k \frac{p(i, k)p(j, k)}{p_x(i)p_y(k)}$$

Equation 14 Haralick maximal correlation coefficient

$$HXY = - \sum_i \sum_j p(i, j) \log(p(i, j))$$

$$HXY1 = - \sum_i \sum_j p(i, j) \log\{p_x(i)p_y(j)\}$$

$$HXY2 = - \sum_i \sum_j p_x(i)p_y(j) \log\{p_x(i)p_y(j)\}$$

Equation 15 logs used in Haralick's information measures of correlation and maximal correlation coefficient

Because the values of the GLCM change, as the distance d and the orientation θ change, the values of the features extracted from the GLCM also change. To make the features rotation invariant for a given distance d all features for all four orientations of 0° , 45° , 90° and 135° degrees are calculated and then averaged out. Also, the range of each such quartet of features is taken as an extra step to obtain more information from the 4 GLCMs.

2.3.2 Gray level difference method

The gray level difference method (GLDM) is a statistical method that is based on absolute differences between pairs of pixels. For a given displacement $\delta = (\Delta x, \Delta y)$, where Δx and Δy are integers, each element $f_{\delta}(x, y)$ of the GLDM equals to $|f(x, y) - f(x + \Delta x, y + \Delta y)|$ where $f(x, y)$ is the intensity value of the image at position (x, y) [124].

The GLDM results in a vector constructed from the sorted in increasing order corresponding absolute gray level difference probabilities for each pair of elements [121]. If the probability values are skewed to the right of the vector the texture elements of the image are coarse and their intensity variation small and conversely, if the probabilities are skewed to the left the texture elements are fine and their intensity variation large.

NaN	1	2	1	NaN
1	2	4	3	1
1	4	4	2	NaN
1	2	4	2	NaN
NaN	1	2	1	NaN

Figure 4 Instance of calculating the GLDM for horizontal pairs.

intensity	0	1	2	3
differences				
frequencies	1	7	5	1

Figure 5 There are 5 horizontal pairs with gray level absolute difference 2.

Similar to the GLCM the orientation of the pixel pairings is given by an angle θ . So to make the features rotation invariant, for a given distance d all features for all four orientations of 0° , 45° , 90° and 135° degrees are calculated and then are averaged out.

NaN	1	2	1	NaN
1	2	4	3	1
1	4	4	2	NaN
1	2	4	2	NaN
NaN	1	2	1	NaN

Figure 6 Instance of calculating the GLDM for diagonal pairs (450).

intensity	0	1	2	3
differences				
frequencies	4	3	2	3

Figure 7 There are 4 diagonal pair (450) with gray level absolute difference 0.

Also, again in similar fashion to GLCM, the range of every quartet of features is taken as an extra step to obtain more information from the 4 GLDMs. Further comparisons and analysis of spread measures of different orientations can give indications for the directionality of the textures.

Another approach proposed in [124] is to take the differences of average gray levels instead of single pixels. The average gray level can be calculated over neighborhoods whose centers are at a distance d and direction θ from each other.

Some features calculated from the GLDMs that are proposed in the literature [124] [121] are the following:

2.3.2.1 Mean

Mean of the GLDM is small if the gray levels of the texture pixels are not too different and large if there is a high level of texture diversity.

$$f_1 = \left(\sum_i i * p(i) \right) / n$$

Equation 16 GLDM mean

2.3.2.2 Angular second moment

Angular second moment or energy that measures the homogeneity of gray levels and it is calculated from the sum of the squares of the entries of the GLDM. If an image is smooth then ASM is large because the values of GLDM are less uniformly distributed and there are a few large frequencies present. If the GLDM is populated by a lot of similar values then the ASM is small.

$$f_2 = \left(\sum_i p(i)^2 \right) / \left(\sum_i p(i) \right)^2$$

Equation 17 GLDM angular second moment or energy

2.3.2.3 Contrast

Contrast or inertia is a measure of intensity contrast between pixels. In the case of the GLDM it is higher if the large values are concentrated in the higher end of the sorted gray level difference vector. It is calculated by summing all the frequencies of the GLDM after weighting them in favor of the pairs with higher intensity difference.

$$f_3 = \sum_i i^2 * p(i)$$

Equation 18 GLDM Contrast or inertia

2.3.2.4 Inverse difference moment

Inverse difference moment or local homogeneity is a measure inversely proportional to the contrast of the image. Images with small local intensity variations have a large amount of local homogeneity. In the case of the GLDM it is higher if the large values are concentrated in the lower end of the sorted gray level difference vector.

$$f_4 = \left(\sum_i p(i) / (1 + i^2) \right)$$

Equation 19 GLDM Inverse difference moment or local homogeneity

2.3.2.5 Entropy

Entropy is a measure of how evenly energy is distributed and is related to the contrast of an image. The smoother the image the lowest the entropy value. In essence, the entropy calculation based on the GLDM takes into consideration the repetition of differences in intensity pairs and therefore gives a measure of the gradient of the texture. Low entropy means more smooth gradient or no significant change in gray levels and higher entropy means more randomness in the structure of the texture.

$$f_5 = - \sum_i p(i) * \log p(i)$$

Equation 20 GLDM entropy

2.3.3 Gradient matrix

Gradient matrix (GradM) features are introduced in [5] and are constructed by calculating the local gradient of each pixel as a function of the differences between the gray levels of its vertically and horizontally neighboring pixels. The resulting GradM contains the values of the absolute gradient at each pixel of a ROI, excluding its boundaries.

A	B	C	D	E
F	G	H	I	J
K	L	M	N	O
P	Q	R	S	T
U	V	W	X	Y

Figure 8 ROI neighborhood

$$Grad = \sqrt{(W - C)^2 + (O - K)^2}$$

Equation 21 The gradient calculation for the Figure 8 ROI neighborhood

The parameters mentioned in the literature [5] [121] to describe the GradM are the following:

2.3.3.1 Mean

Mean of the GradM is small if the texture is smooth and large if its gray levels fluctuate.

$$f_1 = \frac{1}{N} \sum_{ij} p(i, j)$$

Equation 22 GradM mean

2.3.3.2 Variance

Variance quantifies the amount of difference in gray levels between small pixel groups over the whole texture and it is higher when the pixel groups vary greatly.

$$f_2 = \frac{1}{N} \sum_{ij} (p(i,j) - f_1)^2$$

Equation 23 GradM Variance

2.3.3.3 Skewness

Skewness is a measure of the asymmetry of the variance of the texture about its mean gray level.

$$f_3 = \frac{1}{N * \sqrt{f_2}^3} \sum_{ij} (p(i,j) - f_1)^3$$

Equation 24 GradM skewness

2.3.3.4 Kurtosis

Kurtosis measures the sharpness of the peaks of the distribution of the difference in gray levels between small pixel groups over the whole texture. It's larger when the texture is comprised of a lot of texture primitives that vary greatly in grey levels.

$$f_4 = \frac{1}{N * \sqrt{f_2}^4} \sum_{ij} (p(i,j) - f_1)^4$$

Equation 25 GradMKurtosis

2.3.3.5 Percentage of nonzero gradient

The last GradM feature is the percentage of pixel neighborhoods with nonzero gradient and it gives a general idea about the difference in gray levels between small pixel groups of the texture as a whole.

2.3.4 Texture feature coding method

Texture feature coding method (TFCM) is a TA method that was introduced in [125]. It transforms a gray level image into a feature map whose elements are texture feature numbers (TFN), the texture feature numbers matrix (TFNM).

The relation of a pixel with its 8 neighbors defines the TFNM value of the pixel. Four cases are examined for each pair of neighbors; a) horizontal neighbors, b) vertical neighbors, c) main diagonal neighbors and d) secondary diagonal neighbors. For each of these cases one triplet of values is produced, the first value is the leftmost pixel or the bottommost for the vertical neighbors, the second is the central pixel and the third the remaining neighbor. A threshold number Δ is also considered. The triplets are coded with different numbers depending on their relative values; the code is a) the number 1 if the absolute difference between the neighbors and the central pixel is less than Δ , b) the number 2 if the absolute difference between one of the neighbors and the central pixel is less than Δ and with the remainder neighbor is more than Δ , c) the number 3 if the difference of one of the neighbors and the central pixel is more than Δ and with the other less than $-\Delta$ and d) the number is 4 if both neighbors have difference with the central pixel more than Δ or less than $-\Delta$.

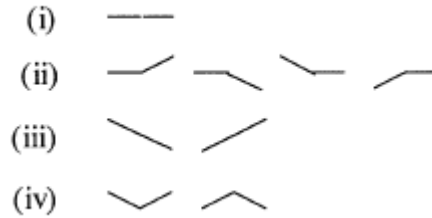


Figure 9 Eachgroup of relative gray level of the triplets has its own code number

Then the codes of the triplets are divided into two pairs, one is the vertical and horizontal neighbors and one is the diagonal neighbors. Each possible code pair, without taking into account pairing order, is given another code number as shown in Figure 10.

		scan line 1			
		(i)	(ii)	(iii)	(iv)
scan line 2	(i)	1	2	3	4
	(ii)	2	5	6	7
	(iii)	3	6	8	9
	(iv)	4	7	9	10

Figure 10 Each pair, regardless of order, has its own code number

The next step is the multiplication of the codes of the pairs to get the TFN of the central pixel. Finally the TFNM is used to generate a TFNM histogram and a TFNM co-occurrence matrix which in turn, are used to produce texture feature descriptors useful for classification.

2.3.4.1 Coarseness

The coarseness value is taken directly from the last bin of the TFNM histogram which corresponds to the frequency of the value 41 in the TFNM. A pixel with TFN value of 41 at the center of a 3x3 neighborhood indicates drastic change in its 8-connectivity. The total number of such neighborhoods is a good indication of texture coarseness.

$$f_1 = \sum_x \sum_y p_{\Delta} * (41)$$

Equation 26 TFCM coarseness

2.3.4.2 Homogeneity

The homogeneity value is taken directly from the first bin of the TFNM histogram which corresponds to the frequency of the value 0 in the TFNM. A pixel with TFN value of 0 at the center of a 3x3 neighborhood indicates almost no change in its 8-connectivity. The total number of such neighborhoods is a good indication of texture homogeneity.

$$f_2 = \sum_x \sum_y p_{\Delta} * (0)$$

Equation 27 TFCM homogeneity

2.3.4.3 Mean convergence

Mean convergence is a feature descriptor that indicates how close the texture approximates the mean.

$$f_3 = \sum_{n=0}^{41} \frac{|np_{\Delta^*}(n) - \mu_{\Delta^*}|}{\sigma_{\Delta^*}}$$

Equation 28 TFCM mean convergence

2.3.4.4 Variance

Variance measures the deviation of TFNs from the mean.

$$f_4 = \sum_{n=0}^{41} (n - \mu_{\Delta^*})^2 p_{\Delta^*}(n)$$

Equation 29 TFCM variance measures

2.3.4.5 Code entropy

Code entropy measures the randomness of TFNs. A small value in code entropy signifies less randomness and a smoother texture.

$$f_5 = - \sum_{i=0}^{41} \sum_{j=0}^{41} p_{\Delta^*}(i, j | d, \theta) \log p_{\Delta^*}(i, j | d, \theta)$$

Equation 30 TFCM code entropy

2.3.4.6 Code similarity

Code similarity assesses the density of the same TFNs in a 3x3 neighborhood. The value of the code similarity is higher if there are a lot of 3x3 neighborhoods with constant TFNs.

$$f_6 = \sum_{i=1}^{41} p_{\Delta^*}^2(i, j|d, \theta)$$

Equation 31 TFCM code similarity

2.3.4.7 Resolution similarity

Resolution similarity provides information about the joint probability of a pixel at (x,y) with TFN i at $\Delta = 0$ and j at Δ^* . If the two TFNs have a lot of differences then the resolution similarity is lower and the texture is smoother.

$$f_7 = \sum_x \sum_y \frac{p(i, j; x, y)}{1 + (i - j)^2}$$

Equation 32 TFCM Resolution similarity

2.3.5 Run length matrix

Run length matrix (RLM) is an NxM matrix derived from a grayscale image with N being the max length in pixels that a line can have in the image in a given direction and M the max gray level value of the image. Each (i, j) element of the RLM is a number that represents the amount of consecutive, collinear pixel runs with length j and gray level i. For a given image, an RLM can be calculated for runs having any given direction. The following example shows a 5x5 ROI having four gray levels (1-4) and the resulting RLMs for the four principal directions.

2.3.5.1 Short run emphasis

Short run emphasis is the division of each run length value by the length of the run squared and then normalized over the total number of runs in the image. The more short runs that are present in the image the larger this value becomes.

$$f_1 = \sum_{i=1}^{N_v} \sum_{j=1}^{N_r} \frac{p(i, j)}{j^2} \bigg/ \sum_{i=1}^{N_v} \sum_{j=1}^{N_r} p(i, j)$$

Equation 33 RLM short run emphasis

2.3.5.2 Long run emphasis

Long run emphasis is the multiplication of each run length value by the length of the run squared and then normalized over the total number of runs in the image. The more long runs that are present in the image the larger this value becomes.

$$f_2 = \frac{\sum_{i=1}^{N_v} \sum_{j=1}^{N_r} j^2 p(i, j)}{\sum_{i=1}^{N_v} \sum_{j=1}^{N_r} p(i, j)}$$

Equation 34 RLM long run emphasis

2.3.5.3 Gray level non-uniformity

Gray level non-uniformity distribution, is the sum of the squares of the number of run lengths for each gray level normalized over the total number of runs in the image. This measures the gray level non-uniformity of the image. When runs are equally distributed throughout the gray levels, the value is low with high run length values contributing more to it.

$$f_3 = \frac{\sum_{i=1}^{N_v} \left(\sum_{j=1}^{N_r} p(i, j) \right)^2}{\sum_{i=1}^{N_v} \sum_{j=1}^{N_r} p(i, j)}$$

Equation 35 RLM gray level non-uniformity - distribution

2.3.5.4 Run length non-uniformity

Run length non-uniformity - distribution, is the sum of the squares of the number of run lengths for each run length normalized over the total number of runs in the image. This measures the non-uniformity of the run lengths. If the runs are equally distributed throughout the lengths, the function will have a low value with large run counts contributing more to it.

$$f_4 = \frac{\sum_{i=1}^{N_v} \left(\sum_{j=1}^{N_r} p(i, j) \right)^2}{\sum_{i=1}^{N_v} \sum_{j=1}^{N_r} p(i, j)}$$

Equation 36 RLM Run length non-uniformity - distribution

2.3.5.5 Run percentage

Run percentage is the ratio of the total number of runs to the total number of possible runs if all runs were one pixel long. It has its lowest value for images with the most linear structure.

$$f_5 = \sum_{i=1}^{N_v} \sum_{j=1}^{N_r} p(i,j)/P$$

Equation 37 RLM Run percentage

2.3.6 Fractal features

The concept of fractal dimension (FD) in TA is usually used to provide an indicator of surface roughness. For a fractal set the Hausdorff-Besicovitch dimension is strictly greater than its topological dimension [3] and it can be used to characterize a texture even though two or more different textures can share the same FD [126].

The box-counting method is a widely used method to approximate the FD of a texture, as it is quick to calculate and can be used on texture patterns with or without similarity. First the texture is converted to a surface with two dimensions indicating the positions of the pixels, as they do in the texture image, and the third dimension is the intensity levels of the pixels. Then, the surface space is partitioned into square boxes of equal size. All the boxes that are at least partially under the surface are counted and the process is repeated with different box sizes with the change in size being the magnification index for every stage. The log of the boxes counted versus the log of the corresponding measuring index is plotted on a graph and then a line is fitted on it. The slope of the fitted line is the FD of the texture.

$$D = \frac{\log(N_r)}{\log(1/r)}$$

Equation 38 The approximation of the fractal dimension D.

Where N_r is the number of boxes for a given box scale and r the measuring index for that scale.

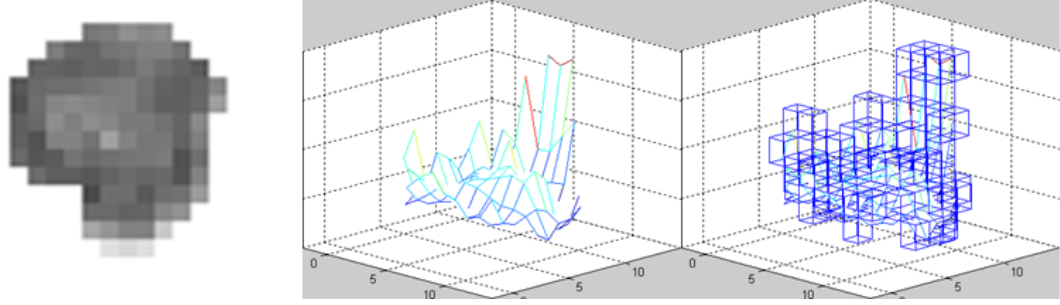


Figure 11 The original texture (left) is converted to a 3D mesh (middle) and then enclosed in boxes of a particular size 'r' (right) that shrinks iteratively.

Here, a variation of the box counting method is used, the differential box counting method. The difference with the original method is that the boxes that count towards the total number are those that are between the minimum and maximum intensity values in any given stack of boxes as this way of counting gives better approximation especially when there is sharp gray level variation in neighboring pixels in the texture [127].

$$N_r = \sum_{i,j} n_r(i,j)$$

Equation 39 The counting of boxes in differential box counting.

Where $n_r = L - K + 1$ and L, K are the indexes of the boxes between the minimum and maximum intensity pixels.

The six features extracted using the original image along with various preprocessed images are proposed in [128].

2.3.6.1 FD of the original image

The FD of the original image is computed by overlapping windows of size $(2W+1) \times (2W+1)$, so at point (i, j) the value $I_1(i, j)$ is

$$I_1(i, j) = FD\{I(i + l, j + k); -W \leq l, k \leq W\}$$

Equation 40 FD of original image

2.3.6.2 FD of high gray value image

The gray level values of the original image pixels that are lower than a value L are replaced with zero and from the rest L is subtracted. $L = g_{\min} + av/2$, where g_{\min} the minimum gray level value of the image and av the average gray level value of the image. The FD of the resulting image is calculated normally.

$$I_2(i,j) = \begin{cases} I_1(i,j) - L & \text{if } I_1(i,j) > L \\ 0 & \text{otherwise} \end{cases}$$

Equation 41 High gray-value level image

2.3.6.3 FD of low gray value image

The gray level values of the original image pixels that are higher than a value L are replaced by that value and the rest stay unchanged. $L = 255 - (g_{\max} - av/2)$, where g_{\max} the minimum gray level value of the image and av the average gray level value of the image. The FD of the resulting image is calculated normally.

$$I_3(i,j) = \begin{cases} L & \text{if } I_1(i,j) > L \\ I_1(i,j) & \text{otherwise} \end{cases}$$

Equation 42 Low gray-value level image

2.3.6.4 FD of horizontally smoothed image

After smoothing the image in the horizontal direction, its FD is calculated normally. If the texture of the image is highly oriented horizontally its FD will be substantially different than the FD of the original image.

$$I_4(i,j) = \frac{1}{2w+1} \sum_{k=-w}^w I(i,j+k)$$

Equation 43 Smoothing an image horizontally with a window of size $2w$.

2.3.6.5 FD of vertically smoothed image

After smoothing the image in the vertical direction, its FD is calculated normally. If the texture of the image is highly oriented vertically its FD will be substantially different than the FD of the original image.

$$I_5(i, j) = \frac{1}{2w + 1} \sum_{k=-w}^w I(i + k, j)$$

Equation 44 Smoothing an image vertically with a window of size 2w.

2.3.6.6 FD of smoothed image

To obtain the last FD feature we smooth the image by averaging four neighboring pixels and then calculate the FD as before.

$$I_6(i, j) = \frac{1}{4} \sum_{i=1}^2 \sum_{j=1}^2 I(i, j)$$

Equation 45 Smoothing an image by averaging 4 neighboring pixels.

3 Validation work

As mentioned in chapter 2 we chose in this thesis to investigate the possible use of TA in pancreatic MRI images in order to assess its discriminatory power for differentiating benign from malignant image regions. In this chapter we explain in detail the dataset used and the results with the proposed methodology.

3.1 Dataset acquisition protocol and post processing

All examinations were performed at 1.5T (MagnetomAvanto, Siemens Healthcare, Erlangen, Germany) with a 12-channel body and spine matrix coil combination. All patients underwent single-shot spin-echo echo-planar imaging DWI of the pancreas with 8 b-values under free-breathing. In order to maintain sufficient signal-to-noise ratio, 5 averages were chosen. Coronal T2-HASTE images were obtained before the DWI sequences for optimal slice positioning. No intravenous contrast agent was used.

The post-processing analysis was performed using the open-source UMMDiffusion plugin for use with OsiriX.25

One radiologist with 6 years of experience in pancreatic imaging annotated carefully multiple ROI at all slices, in order to define the tumor and non-tumorous parenchyma both up and downstream. There was an effort to avoid the inclusion of large vessels but to include main pancreatic duct and areas of possible necrosis/cystic changes. The DWI sequence chosen for ROI annotation was the image series where the tumor was best visualized. For optimal ROI positioning, apart from DWI all other available images (i.e. T2-HASTE and MDCT) were taken into consideration to account for the relatively low spatial resolution of DWI images.

The DWI parametric image maps that were evaluated and the corresponding formula used were:

- i. ADC from the monoexponential model, according to:

$$S(b) = S_0 \exp(-b \cdot \text{ADC})$$

- ii. D, D* and f from the biexponential fit, according to:

$$S(b) = S_0 [(1-f) \exp(-D \cdot b) + f \exp(-b \cdot D^* - b \cdot D)]$$

- iii. K and D(k) from the non-gaussian kurtosis fit, according to:

$$S(b) = S_0 \exp(-b \cdot D(k) + K/6 \cdot b^2 \cdot D(k)^2),$$

where S(b) is the signal intensity (SI) at a given b-value, S₀ the SI without any diffusion weighting gradient (b=0 s/mm²), ADC the apparent diffusion coefficient, D the true diffusion coefficient, D* the pseudodiffusion coefficient, f the perfusion fraction, D(k) is the corrected –for kurtosis– diffusion coefficient, and K the kurtosis coefficient. The kurtosis coefficient expresses the grade of deviation from the Gaussian distribution and is a unitless parameter, whose value may be either 0 (expressing perfect Gaussian distribution) or higher. Kurtosis effects were classified as minimal (K<0.5), intermediate (0.5<K<1) or substantial (K>1).

3.2 Texture analysis and feature extraction

The dataset used in this work is a set of 14 pairs of volumes of interest (VOIs) (annotated by a specialist) from DW-MRIs of pancreatic tissue from 14 patients diagnosed with pancreatic adenocarcinoma. Each pair contains one VOI depicting tumorous tissue and one depicting normal appearing tissue from the same patient and each one is comprised of 1 to 15 slices depending on the size of the region of interest.

3.2.1 Number of DWI metrics maps

From each slice a feature image representation is generated. These representations are the original intensity values map I , the 3 different parameter image maps obtained from the IVIM model D , D^* , f and their 2 products $f \times D$, $f \times D^*$, leading to a total of 6 representation maps per slice.


[illegible]

Figure 12 Each DW-MRI is a set of slices representing a 3D volume

3.2.2 Number of different non-ROI pixel values setting

In a preprocess step, the metrics maps are converted into grayscale images. First the map values are rescaled to rounded values from 0 to 255 as in Figure 13.

NaN	NaN	NaN	NaN	NaN	NaN	NaN	NaN
NaN	NaN	NaN	NaN	0.00246	NaN	NaN	NaN
NaN	NaN	NaN	0.00166	0.00171	0.00162	NaN	NaN
NaN	NaN	0.00143	0.0013	0.00152	0.00156	NaN	NaN
NaN	NaN	0.00117	0.00151	0.00162	0.00117	0.00182	NaN
NaN	NaN	0.00135	0.00125	0.00153	0.00164	0.00125	NaN
NaN	NaN	0.0013	0.00131	0.00144	0.00155	0.00097	NaN
NaN	0.00133	0.00113	0.00113	0.00135	0.00179	NaN	NaN
NaN	0.00117	0.00134	0.00111	0.00151	0.00179	NaN	NaN
NaN	0.00101	0.00098	0.00088	0.00147	0.00174	NaN	NaN
NaN	NaN	0.00103	0.00119	0.00188	NaN	NaN	NaN
NaN	NaN	NaN	NaN	NaN	NaN	NaN	NaN
NaN	NaN	NaN	NaN	NaN	NaN	NaN	NaN




NaN	NaN	NaN	NaN	NaN	NaN	NaN	NaN
NaN	NaN	NaN	NaN	255	NaN	NaN	NaN
NaN	NaN	NaN	126	134	119	NaN	NaN
NaN	NaN	89	68	103	110	NaN	NaN
NaN	NaN	47	102	119	47	152	NaN
NaN	NaN	76	60	105	123	60	NaN
NaN	NaN	68	69	90	108	15	NaN
NaN	73	40	40	76	147	NaN	NaN
NaN	47	74	37	102	147	NaN	NaN
NaN	21	16	0	95	139	NaN	NaN
NaN	NaN	24	50	161	NaN	NaN	NaN
NaN	NaN	NaN	NaN	NaN	NaN	NaN	NaN
NaN	NaN	NaN	NaN	NaN	NaN	NaN	NaN

Figure 13 Each slice is rescaled to the range {0, 255}.

Next we find the minimum pixel value of the ROI and set the surrounding non-ROI pixels to this value, additionally we enclose it in its minimum bounding box. This is a method proposed in [30], as non-ROI pixels might affect the outcome of a pixel based TA method when calculating the values of the pixels on the edge of the ROI. In the present work we expand on this idea to exploit any further potential benefits from setting the non-ROI pixels to different values. The area inside the bounding box is copied several times and the non-ROI pixels of each copy are set to the maximum, the median and the mean values of the ROI. With the addition of another copy of the bounded areas whose non-ROI pixels have their original values, i.e. are treated as empty pixels, the number of ROIs is increased by a factor of 5 and are saved as grayscale texture images.

NaN	NaN	NaN	NaN	NaN	NaN	NaN	NaN
NaN	NaN	NaN	NaN	255	NaN	NaN	NaN
NaN	NaN	NaN	126	134	119	NaN	NaN
NaN	NaN	89	68	103	110	NaN	NaN
NaN	NaN	47	102	119	47	152	NaN
NaN	NaN	76	60	105	123	60	NaN
NaN	NaN	68	69	90	108	15	NaN
NaN	73	40	40	76	147	NaN	NaN
NaN	47	74	37	102	147	NaN	NaN
NaN	21	16	0	95	139	NaN	NaN
NaN	NaN	24	50	161	NaN	NaN	NaN
NaN	NaN	NaN	NaN	NaN	NaN	NaN	NaN



				86	86	86	86	86	86	86	86	86	86
				86	86	86	86	255	86	86	86	86	86
			0	86	86	86	126	134	119	86	86	86	86
		0	86	86	89	68	103	110	86	86	86	86	86
	255	0	86	86	47	102	119	47	152	86	86	86	86
76	255	0	86	86	76	60	105	123	60	86	86	86	86
76	255	0	86	86	68	69	90	108	15	86	86	86	86
76	255	0	86	73	40	40	76	147	86	86	86	86	86
76	255	0	86	47	74	37	102	147	86	86	86	86	86
76	255	0	86	21	16	0	95	139	86	86	86	86	86
76	255	0	86	86	24	50	161	86	86	86	86	86	86
76	255	0	86	86	86	86	161	86	86	86	86	86	86
76	255	0	0	0	24	50	161	0	0	0	0	0	0
76	255	0	0	0	24	50	0	0	0	0	0	0	0
76	255	255	255	24	50	161	255	255	255	255	255	255	255
76	255	255	255	24	50	161	255	255	255	255	255	255	255
76	76	76	76	76	76	76	76	76	76	76	76	76	76
76	76	76	76	76	76	76	76	76	76	76	76	76	76

Figure 14 Copies of the ROI are made and the “nan” values are replaced by the median, mean, maximum and minimum value of the ROI.

3.2.3 Number of TA methods output maps and number of neighborhood sizes N

The TA methods used in this work are the GLCM, GLDM, GradM, TFCM and FD and they have been described above. The input of each method is a grayscale texture image and the output is one or several image maps of texture features – one map for each feature of each TA method. The total number of the feature imagemaps for each texture image is 35;

- 11 from the mean and 11 from the value ranges of all four orientations of GLCM,
- 5 from the means and 5 from the value ranges of all four orientations of the GLDM maps,
- 1 from the GradM,
- 1 from the TFCM,
- 1 from the FD.

The feature image maps are 2D matrixes with the same size as the texture images. Each (i, j) value on a feature map is calculated from an $N \times N$ texture neighborhood centered on the pixel at position (i, j). While N can be of any size, in this work it is given each of the four values; 3, 5, 7 and 9. The texture image is padded from all sides by $N/2$ so no neighborhood has elements outside the image. The value of the padding pixels is the same as the non-ROI pixels of the image.



Figure 15 Fromleft to right, DW-MRI slice of a pancreas ROI, its GradM map and its TFCM map

To better evaluate the usefulness of the results we also calculate a set of 8 image maps based on statistical measures of the intensity and metric maps without any TA, namely

the kurtosis, mean, median, energy, range, skewness, variance and coefficient of variation. These maps are called the 'Raw Value' maps and increase the total number of maps derived from a single texture image to 43.

Each feature map is then converted to a feature vector by taking, in no particular order, the values that correspond only to ROI pixels. The final number of feature image vectors generated is based on the following formula;

$$\text{Number of feature image vectors} = [\text{number of metrics maps}] \times [\text{number of different non-ROI pixel values setting}] \times [\text{number of TA methods output maps}] \times [\text{number of neighborhood sizes}]$$

In this work the corresponding numbers are;

$$6 \times 5 \times 43 \times 4$$

For a total of 5160 feature vectors per slice.

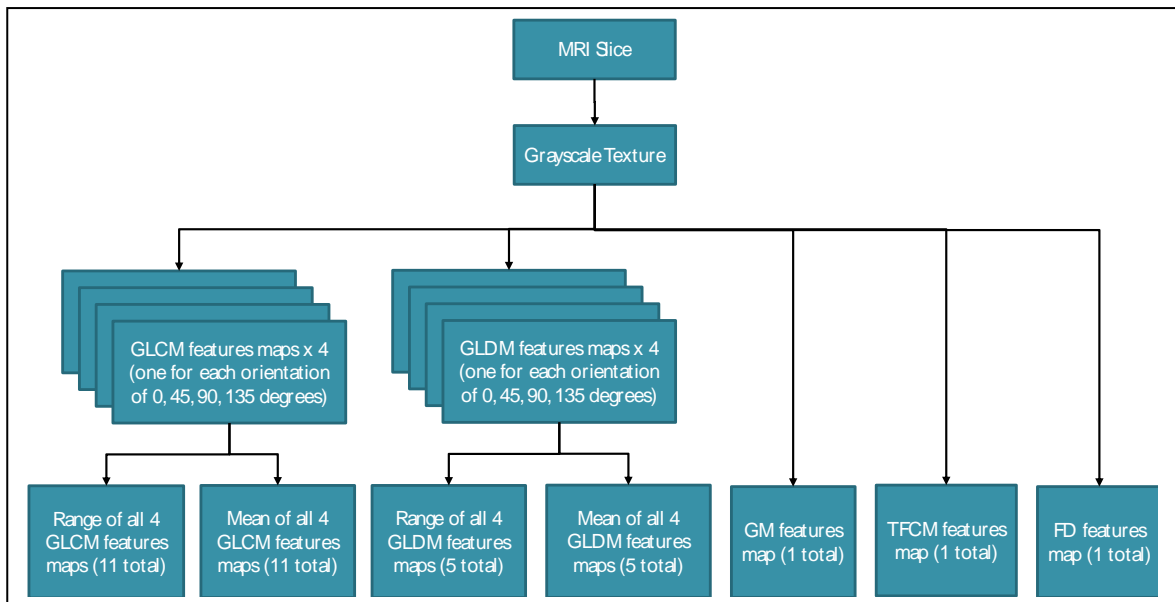


Figure 16 Workflow from MRI to TA feature maps

3.3 Classification and statistical analysis methods

Each of the feature vectors derived from the pixel based TA is finally described by 10 statistical values. These values are; mean, variance, median, standard deviation, 5th percentile, 30th percentile, 70th percentile, 95th percentile, skewness and kurtosis. At this stage we have a vector of length 51600 that represents each patients' MRI. Then we create a table with rows that consist of the aforementioned vectors and, subsequently, columns that each contains a vector of a specific statistical variable from all the MRI maps and length equal to the number of patients.

An example of a statistical variable is the “D_difm_mn ENTR_VMean_3_Bmax” as shown in Table 1. It is calculated from the MRI metric diffusion (D), with the TA method GLDM (difm), taking the mean (mn) of the 4 entropy feature maps (entr) - to make the feature map orientation independent - then take the mean of the resulting feature map (VMean) with the map being calculated on a per pixel bases from 3x3 pixel blocks (3) while all the non-ROI pixels are set to the maximum value of the ROI (Bmax).

Table 1 An example column from the table that contains all the statistical values that represent each patients' MRI..

Patients	D_difm_mn ENTR_VMean_3_Bmax
Acr_n	0.855494491
Acr_t	1.041458595
As_n	0.848710686
As_t	1.171773913
Ed_n	0.657246952
Ed_t	1.23035907
Ep_n	0.78201723
Ep_t	1.055340078
Ga_n	0.80003573
Ga_t	1.248953251

Ke_n	0.725246384
Ke_t	1.174616854
Liw_n	0.91738745
Liw_t	1.087597727
Lsf_n	0.680878462
Lsf_t	1.101524775
Mbf_n	1.199003802
Mbf_t	1.258817717
Pam_n	0.950032274
Pam_t	1.180225323
Ragp_n	0.918033401
Ragp_t	1.163491269
Rkbj_n	0.89892102
Rkbj_t	1.236234038
Ro_n	0.900045673
Ro_t	1.357901099
Use_n	1.188090214
Use_t	1.306120933

Next we apply several tests to the variables to find out if there are any that can lead to accurate classification according to the ground truth (i.e. cancer or normal tissue).

The first test we applied is the Kruskal-Wallis test [129] which helps to distinguish a subset of variables as the most useful to characterize and classify the data. The test is applied to each variable and the estimated p-values of the test are declared statistically significant at the 1% significance level.

After the Kruskal-Wallis test we employ a leave one patient out (LOPO) method to get another subset of statistically significant variables. Each variable is passed P times through the algorithm described in Figure 17 - where P is the number of patients - and each time one of the patients data is excluded from the sample. The algorithm quickly and naively calculates a value that separates perfectly the classes of a continuous

variable. It is naive because it only works well if there is such a value and if there is not then the value proposed by the algorithm is always worse than what a more robust classification method would provide. In this LOPO method if a variable, by using this algorithm, can classify the P-1 patients' MRI correctly in even one iteration then that variable is marked as significant. At the end of this process, we end up with a second set of 895 variables out of 51600 that provide 100% accuracy with none or, at most, one of the patients excluded from the sample.

M_i , the i_{th} variable vector.

M_{in} , the set of parameters that belong to the normal appearing tissue class in M_i .

M_{it} , the set of parameters that belong to the cancer tissue class in M_i .

$A_i = |\text{maximum}(M_{it}) - \text{minimum}(M_{in})|$

$B_i = |\text{maximum}(M_{in}) - \text{minimum}(M_{it})|$

If $A_i < B_i$ then cutoff point is $CP = (\text{maximum}(M_{it}) + \text{minimum}(M_{in})) / 2$

Figure 17 Algorithm for calculating the cutoff point for the classification of a single metric vector.

A generalized linear regression model is fitted on each variable to obtain good discrimination with a simple but robust classification method that doesn't assume a normal distribution of data and works well with small samples [130]. Receiver operator characteristics (ROC) curves are computed and the corresponding area under the curves (AUCs) are calculated to assess the performance of the variables in predicting the responsiveness of the treatment. The AUC values along with the optimal cutoff value of all ROC curves are reported in a confusion matrix that also contains the number of true positives (TP), true negatives (TN), false positives (FP) and false negatives (FN) and their derivatives; sensitivity, specificity, negative and positive predictive values and accuracy.

4 Results

From the Kruskal-Wallis test on this sample population we get that 44% (22901 out of 51600) of the variables have statistically significant differences between the values that belong to the 'tumor' class and that of the 'normal' class for them to be eligible for further analysis with p-values equal or lower than the 1% significance level.

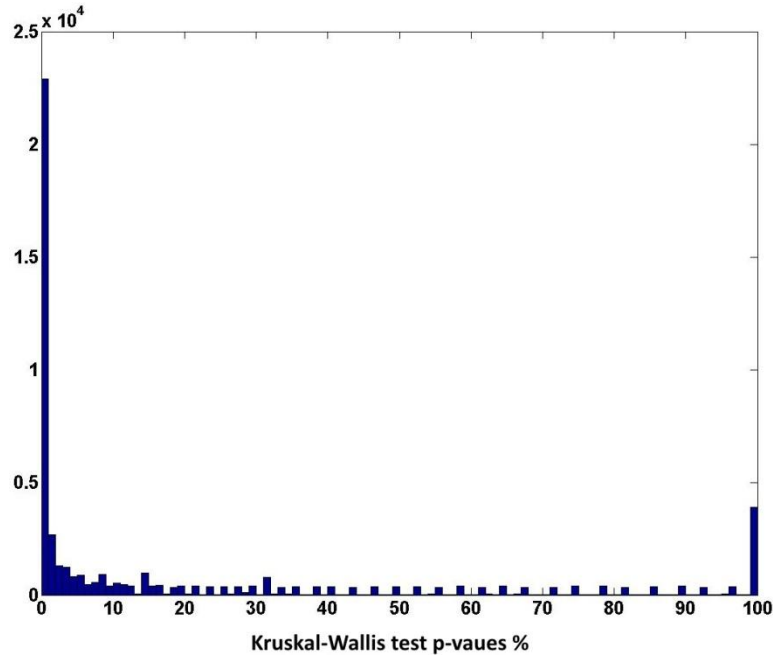


Figure 18 Kruskal-Wallis tests p-values of all the variables

A second subset of 1.7% (895) of the total variables provide perfect classification according to the LOPO method in at least one subsample of the set. The Kruskal-Wallis p-values of this subset are less than the 0.024% significance level. We will not discuss the classification process of this method because as stated previously this method uses a naive algorithm to quickly calculate correctly only the perfectly classifiable variables.

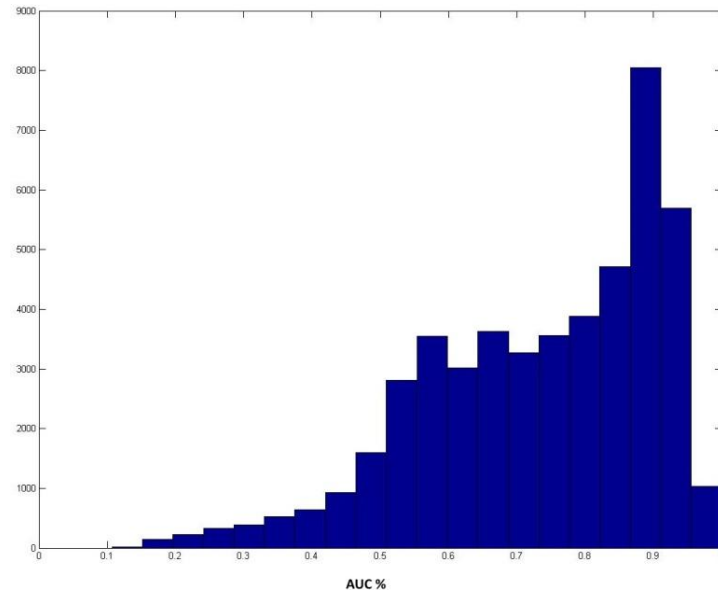


Figure 19 AUC values of variables with non-zero variance - 93% of total number of variables (48085 out of 51600).

Finally, we fit a linear regression model on the variables and we get that 0.06% (30) of the variables provide perfect classification while 16.4% (8473) have AUC above 90% and a Kruskal-Wallis p-value lower than 0.5%. Variables that have values with variance close to 0 are excluded from this test as these contain no useful information and are usually variables that result from feature maps that contain values that are all the same or extremely close to one value. The variables excluded based on this criteria is 7% (3586) of the total variables.

Table 2 Features with 100% AUC from the linear regression model

Method	Map	Block size	Non roi values	Feature	Statistic	AUC	KruskalP	Sens	ACC
GLDM	fDstar	3	mean	rng_nrg	Skewness	100.00%	0.0007%	100.00%	100.00%
Raw Values	Dstar	7	mean	kurt	Variance	100.00%	0.0007%	100.00%	100.00%
Raw Values	Dstar	7	mean	kurt	Std	100.00%	0.0007%	100.00%	100.00%
GradM	D	7	median		Variance	100.00%	0.0007%	100.00%	100.00%
GradM	D	7	median		Std	100.00%	0.0007%	100.00%	100.00%
Raw Values	fD	7	median	skew	5percentile	100.00%	0.0007%	100.00%	100.00%
GLCM	f	9	max	rng_corr	95percentile	100.00%	0.0007%	100.00%	100.00%
Raw Values	Dstar	9	mean	kurt	Variance	100.00%	0.0007%	100.00%	100.00%
GLCM	f	9	mean	rng_entr	Variance	100.00%	0.0007%	100.00%	100.00%
Raw Values	Dstar	9	mean	kurt	Std	100.00%	0.0007%	100.00%	100.00%
GLCM	f	9	mean	rng_entr	Std	100.00%	0.0007%	100.00%	100.00%

Raw Values	Dstar	9	mean	nrg	95percentile	100.00%	0.0007%	100.00%	100.00%
Raw Values	Dstar	9	mean	range	95percentile	100.00%	0.0007%	100.00%	100.00%
Raw Values	Dstar	9	mean	vrnc	95percentile	100.00%	0.0007%	100.00%	100.00%
Raw Values	Dstar	9	mean	vrtn	95percentile	100.00%	0.0007%	100.00%	100.00%
Raw Values	fDstar	9	mean	nrg	95percentile	100.00%	0.0007%	100.00%	100.00%
Raw Values	fDstar	9	mean	range	95percentile	100.00%	0.0007%	100.00%	100.00%
Raw Values	fDstar	9	mean	vrnc	95percentile	100.00%	0.0007%	100.00%	100.00%
Raw Values	fDstar	9	mean	vrtn	95percentile	100.00%	0.0007%	100.00%	100.00%
GradM	D	9	mean		Kurtosis	100.00%	0.0007%	100.00%	100.00%
GLDM	fD	9	nan	rng_hmgnt	Variance	100.00%	0.0007%	100.00%	100.00%
GLCM	fD	9	nan	rng_hmgnt	Variance	100.00%	0.0007%	100.00%	100.00%
GLDM	fD	9	nan	rng_hmgnt	Std	100.00%	0.0007%	100.00%	100.00%
GLCM	fD	9	nan	rng_hmgnt	Std	100.00%	0.0007%	100.00%	100.00%
Raw Values	Dstar	9	nan	nrg	95percentile	100.00%	0.0007%	100.00%	100.00%
Raw Values	fDstar	9	nan	nrg	95percentile	100.00%	0.0007%	100.00%	100.00%
GLCM	l	7	nan	mn_hmgnt	5percentile	100.00%	0.0007%	100.00%	100.00%
GLDM	l	9	nan	rng_mn	Variance	100.00%	0.0007%	100.00%	100.00%
GLDM	l	9	nan	rng_mn	Std	100.00%	0.0007%	100.00%	100.00%
Raw Values	l	9	nan	vrnc	Mean	100.00%	0.0007%	100.00%	100.00%

5 Discussion and Future work

5.1 Discussion

Pancreatic MRI protocols have evolved a lot in the last few years providing images of improved spatial resolution and contrast and better overall image quality [117]. An automatic system for quantitative characterization and subsequent classification of pancreatic MRI in predefined clinical categories could become a valuable Computer Aided Diagnosis tool for assisting the clinician to establish diagnosis or monitor treatment.

The initial steps of such a tool are represented here, with the work being focused around the hypothesis that TA methods can provide the means to classify tissue content from MRI data.

More specifically the null hypothesis we test is:

H_0 : There are no classifiers that can be created so that features extracted from MRI data with the use of specific TA methods are adequate to classify that MRI data in predefined clinical categories.

The alternate hypothesis is:

H_1 : Classifiers can be created so that features extracted from MRI data with the use of specific TA methods are adequate to classify that MRI data in predefined clinical categories.

By using established TA methods we first extract features from an already classified dataset of pancreatic MRIs depicting tumorous and normal appearing tissue and train classifiers on these extracted features. The classifier is a simple linear regression model fitted on each variable so that each one is judged by itself on its ability to adequately classify the MRIs.

After the extraction of the features and their statistical analysis yielding the variables which are vectors that contain one value for each MRI in the dataset, we proceed with testing the results.

A first analysis of the variables is done by applying a Kruskal-Wallis test on them and characterizing as significant those that produced p-values under the 0.1% significance level. As stated above the amount of variables with p-values below the 0.1% significance level are 44% of the total. From these variables we get an even better subset - 29.5% of the total - by fitting them in a linear regression model and focus on the ones that have AUC above 90%. A number of interesting observations can be made with regard to the influence of metric maps and TA methods in the discretization of this subset.

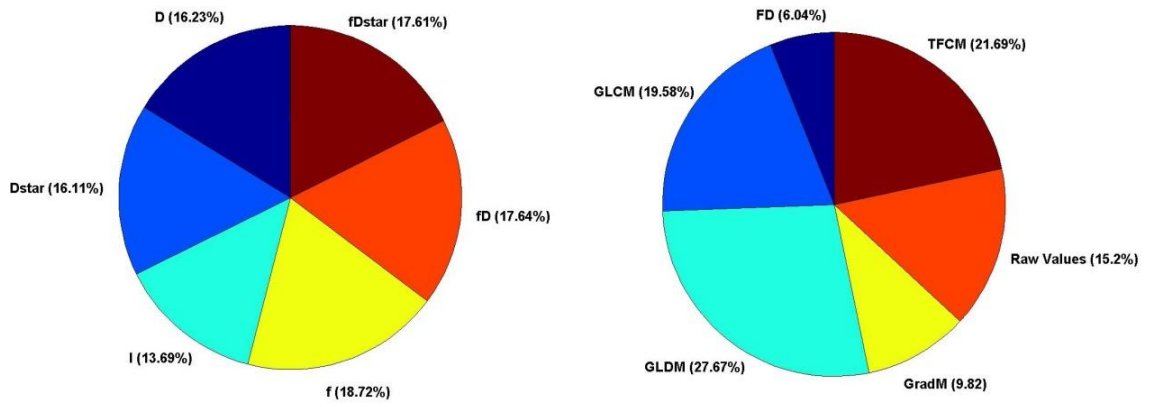


Figure 20 The amounts of MRI Metrics (left) and TA methods (right) that produce variables with Kruskal-Wallis test p -values under the 0.1% and AUCs above 90%.

In Figure 20 on the left pie chart we see that the I, D, D*, f , fD and fD^* maps produce about the same amount of features that classify the variables with AUC above 90%, with a small excess of the f metric maps and with the intensity maps I lagging a bit behind. On the right we see the relative contributions of the TA methods weighted by the number of features each method produces. As stated in chapter 2.3 the methods produce the following number of features; GL produces 8 features, GLCM produces 22 features, GLDM produces 10 features and each of the GradM, TFCM and FD produce 1 feature. The right pie chart shows that the GLDM produces the most variables with AUC above 90%, followed by the TFCM, GLCM and the base case of raw map values. The GradM and FD methods contribute very little in this important variable set.

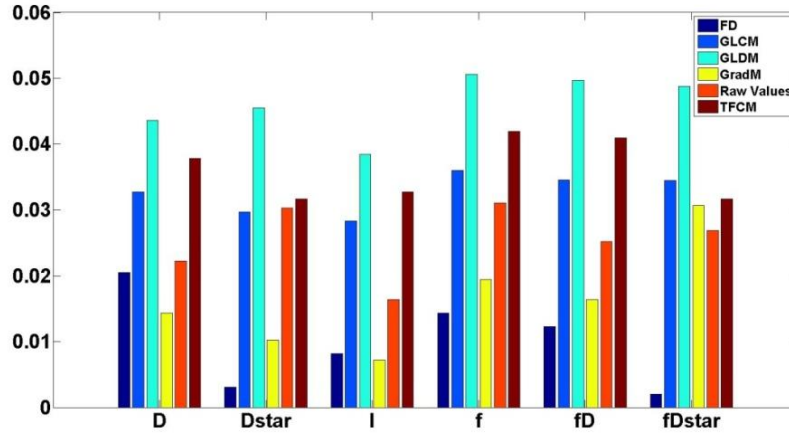


Figure 21 MRI metrics and TA methods with AUC above 90% weighted by the number of features of each TA method

In Figure 21 we see a combination of the two pie charts in Figure 20. Here we see that in almost all cases we get consistently better results from the 5 metric maps than the raw intensity values of the MRIs for all the TA methods. GLDM is contributing more to the variables subset of AUC above 90% in relation to the amount of features it produces followed by GLCM, TFCM and Raw Values while the contribution percentages of FD and GradM fluctuate between very small and comparable with the rest.

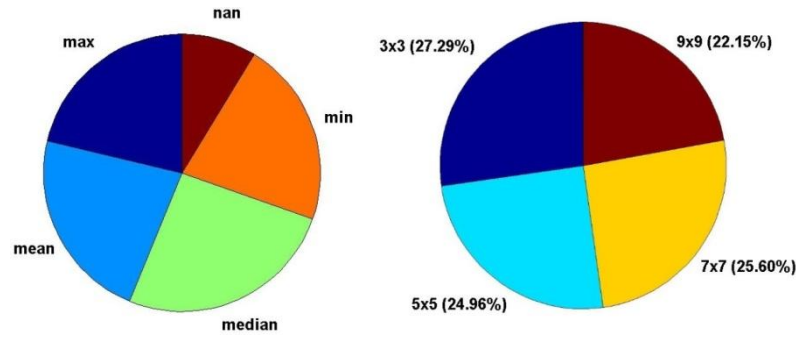


Figure 22 Non-ROI pixel values and block sizes used to generate variables with AUC above 90%.

Figure 22 shows how the neighborhood size and fixing the non-ROI pixels with certain values affect the features. The size of the neighborhood doesn't seem to affect the variables very much with only the 9x9 size lacking a bit compared to the others. Setting the non-ROI pixels to be empty (giving them the “nan” value) produces the less amount

of good variables while the median value of the ROI seems to have a slight edge compared to the rest of the values.

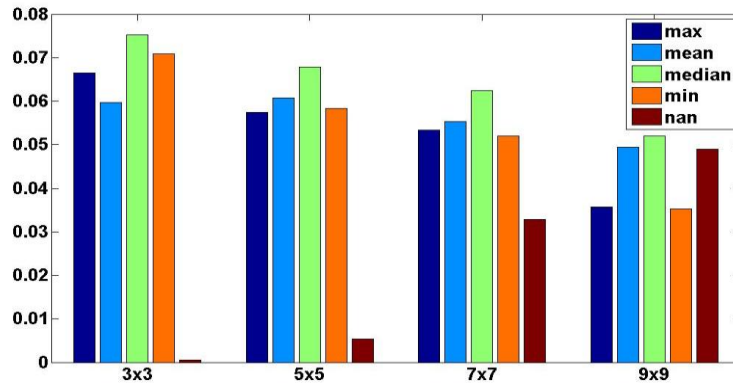


Figure 23 Neighborhood size and non-ROI pixel values in subset of variables with AUC above 90%.

Figure 23 is a combination of the two previous pie charts and clearly shows that when the non-ROI pixels are set to the “nan” value, the number of variables with AUC above 90% increases as the block size is getting larger. However, the total number of the useful variables for the rest of the non-ROI value setting decreases with window size. This shows that using a smaller block size and setting the non-ROI values to something else than “nan” will increase the chances of producing a good classifiable variable while keeping the features map computation time reasonable.

A second subset of variables is comprised of those that classify perfectly the new population samples created by the LOPO method described in paragraph 3.3. This results in 1.7% or 895 variables that can classify all or at most all but one patients correctly. All of these features have a Kruskal-Wallis test p-value under the 0.024% significance level and all of them except one have an AUC of over 91%. This method is quick and naive but it presents the results in a personalized manner as it shows the influence of each patient’s data in the classification process.

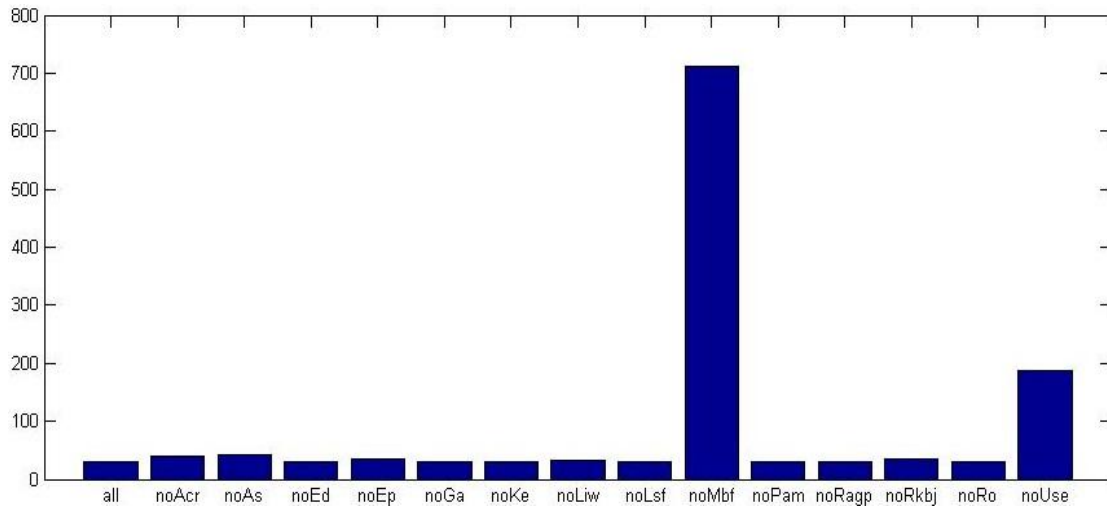


Figure 24 Amount of features that classified the dataset perfectly with the full dataset and after the exclusion of each patient in a leave one patient out method.

In Figure 24 we see the reason why this subset of 895 variables is considered interesting. It shows how many variables classify perfectly the MRIs into tumor and normal appearing tissue on the original sample with all P patients as well as in the P-1 samples created by the exclusion of one patient's data each time. The number 895 is the count of unique variables that perfectly classify the subsets, that is a variable is added only once to the total even if it classifies perfectly more than one P-1 subsamples. We see that for the complete sample and 12 of the P-1 samples the good variables are between 30 and 43 but when patient "Mbf" is excluded the variables are 711 and when patient "Use" is excluded the variables are 188. This could be significant if there is any correlation between this disparity and anything unusual in the clinical history of these patients but it can also be due to the fact that with MRI it's difficult to obtain uniform image quality over a number of images.

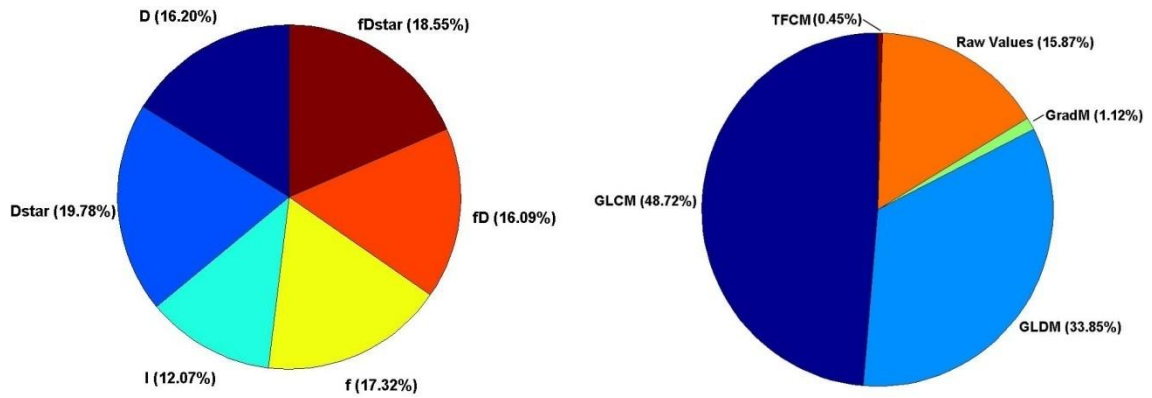


Figure 25 MRI metrics (left) and TA methods (right) in LOPO subset.

In Figure 25 on the left bar chart we can see that the I, D, D*, f , fD and fD^* maps produce about the same amount of features that classify the samples correctly in the LOPO method and on the right that the GLCM provide more of the features followed closely by the GLDM while Raw Values statistics are lagging behind in performance. The TFCM and GradM contribute very little while no DF features are present in the subset.

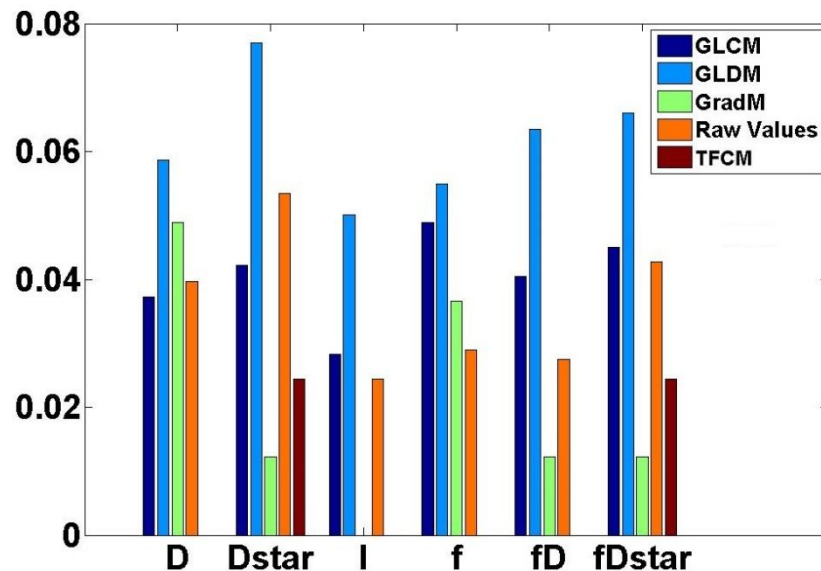


Figure 26 MRI metrics and TA methods in subset 2 weighted by the number of features calculated by each TA method.

In Figure 26 we see a combination of the two piecharts in Figure 25 but with the bars weighted by the number of features extracted by each TA method. Here we see that

GLDM contributes more to the subset, within any kind of map, in relation to the amount of features it extracts, followed by the GLCM and Raw Value statistics while the GradM method with its one feature contributes a lot in the classification of D and f maps. The TFCM method produces a minimal share of the important features and the FD method produces none.

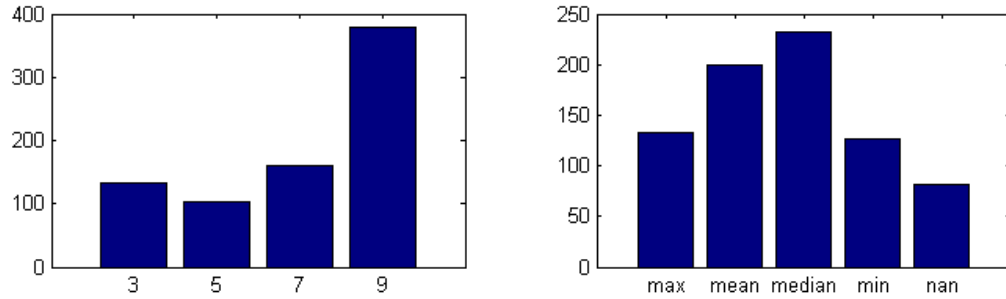


Figure 27 Neighborhood size (left) and non-ROI pixel values (right) in subset 2

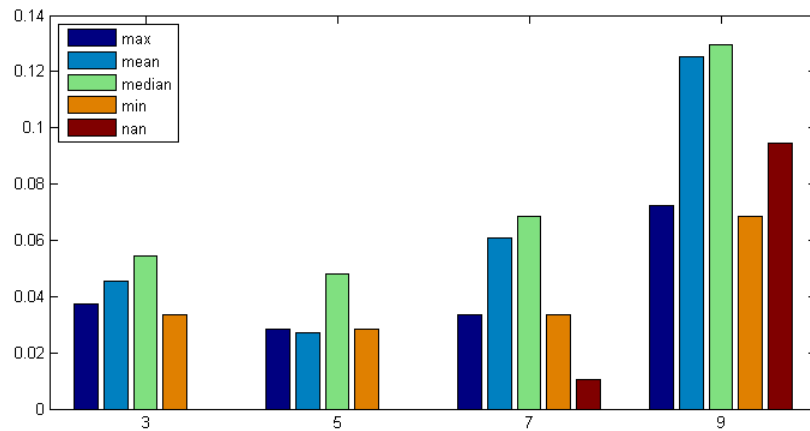


Figure 28 Neighborhood size and non-ROI pixel values in the LOPO subset

Figure 28 shows how the neighborhood size and non-ROI pixel values seems to affect the classification of the variables. Again, as in the first subset, setting the non-ROI pixels to be empty (giving them the “nan” value) and increasing the size of the neighborhood seems to improve the results while setting the median value of the ROI to the non-ROI pixels seems to give a slight edge to the amount of variables that exhibit perfect classification. In contrast to the first subset however the total number of variables for all the non-ROI value setting combinations increases as the block size is

getting larger. This may show that variables that provide perfect classification benefit from larger block sizes but their number is small - 1.7% for this set- so it is possible that this happens by chance due to the large amount of variables. On the other hand there is a large percentage of variables created from smaller block sizes that provide weaker classifiers - Figure 19 shows that 29.5% of the variables of this sample have AUC of over 90% and 84% are above the 50% AUC mark which is what a random classifier would achieve. These percentages suggest that TA has a positive effect towards the correct discrimination of the dataset. A claim that is further supported by Figure 20 where we see that the GLDM, TFCM and GLCM methods create more good features than those we get directly from the raw values of the maps.

In conclusion we reject the null hypothesis as we showed that, at least for the pancreatic MRI sample available, there are features obtained from TA methods that can perfectly classify the patient VOIs, as either depicting normal appearing or tumor tissue. In addition we showed that the majority of the features that don't perfectly classify the samples are themselves medium to strong classifiers, supporting the use of TA as a preprocessing step in MRI classification. Finally we did a personalized analysis to see the influence of each patients' data on the sample and found that most of the patients have the same effect on the results except a few that have more pronounced impact but without any more knowledge about the sample we cannot perform further analysis to understand if there is an underlying biological reason for this or reasons related to the image acquisition process.

5.2 Future work

This thesis focused on the image texture and how we can derive useful measures in order to differentiate between benign and malignant regions in MRI images and used as a case study a dataset of pancreatic tissue MRIs. Our analysis and results clearly showed that there is value in the inclusion of texture metrics of MRI maps in the effort to classify its contents and the potential of TA in discriminating between benign and malignant pancreatic MRIs is demonstrated, but only on a small sample of 14 patients.

For more conclusive results the proposed method should be applied on larger pancreatic MRI datasets in order to verify our results and produce more robust texture descriptors to the research community.

The small number of available samples and the large number of features extracted from them make this classification problem suffer from issues related to the dimensionality. In paragraph 5.1 we suggested and demonstrated that there are ways to find a lot of medium to strong classifiers using the Kruskal - Wallis test and measuring the AUC of the feature variables. A good way to take advantage of the high count of these, good but not perfect classifiers, is to feed them in a boosting algorithm - e.g. Adaboost [131]—in order to create a strong and robust classifier.

Other aspects of future work include:

- More features can be extracted from some of the TA methods used, like the FD from which we can extract multiple features [128] since only one per MRI was extracted here.

- GLCM and GLDM features can have a large range of offset distances effectively changing the “resolution” of the analysis in order to find the relevant texture features in multiple scales automatically as part of the discriminant analysis.

- There are other methods that can be used to extract features from MRI maps. Wavelet transforms [132] and Fourier power spectrum transform [133] are maybe worth investigating and comparing with the methods applied in this thesis. The application of the presented framework can also be generalized to images from other organs and modalities (e.g. CT and PET) in order to provide clinically useful classifiers of normal vs. cancer tissue based on image texture.

Finally because cancer cells occupy 3D space and MRI provide 3D spatial information in the form of multiple vertically aligned 2D slices of an area of interest, any TA methods used should be expanded to extract information not only per slice but take into account vertical interslice relationships as well.

6 Appendix

6.1 Abbreviations

ADC	Apparent Diffusion Coefficient
ASM	Angular Second Moment
AUC	Area Under The Curve
CAD	Computer-Aided Detection
CADe	Computer-Aided Detection
CADx	Computer-Aided Diagnosis
CaP	Prostate Cancer
CMRI	Cardiac MRI
CT	Computed Tomography
D	Diffusion Coefficient
D*	Pseudodiffusion Coefficient
DCE	Dynamic Contrast Enhanced
DW	Diffusion Weighted
f	Perfusion Factor
FD	Fractal Dimension
FN	False Negative
FP	False Positive
GL	Gray Level
GLCM	Co-Occurrence Matrix
GLDM	Gray Level Difference Method
GradM	Gradient Matrix
HR-MRI	High Resolution MRI
IVIM-MRI	Intra-Voxel Incoherent Motion MRI
LOOCV	Leave One Out Cross Validation
LOPO	Leave One Patient Out
MRI	Magnetic Resonance Imagine
mn	Mean
PaC	Pancreatic Cancer
RLM	Run Length Matrix
rng	Range
ROI	Region Of Interest
T1	Longitudinal Relaxation Time
T2	Transverse Relaxation Time
TA	Texture Analysis

TFCM	Texture Feature Coding Method
TFN	Texture Feature Number
TFNM	Texture Feature Numbers Matrix
TN	True Negative
TP	True Positive
US	Ultra Sound
WB-MRI	Whole-Body MRI

7 References

- [1] S. Soman, L. E. and A. S. C., "Textural Kinetics: A Novel Dynamic Contrast-Enhanced (DCE)-MRI Feature for Breast Lesion Classification," *Journal of Digital Imaging*, vol. 24, no. 3, pp. 446-463, 2011..
- [2] R. M. Haralick, K. Shanmugam and Dinstein, "Textural features for image classification," *IEEE Transactions on systems, man and cybernetics*, Vols. SMC-3, no. 6, pp. 610-621, 1973.
- [3] B. B. Mandelbrot, "Self-Affine Fractals and Fractal Dimension," *Physica Scripta*, vol. 32, no. 4, pp. 257-260, 1985.
- [4] D. Nilsson, R. Henriksson and P. Brynolfsson, "ADC texture—An imaging biomarker for high-grade glioma?," *Journal of Digital Imaging*, vol. 24, no. 3, pp. 446-463, 2011.
- [5] R. A. Lerski, K. Straughan, I. R. Schad, D. Boyce, S. Bluml and I. Zuna, "MR Image texture analysis - an approach to tissue characterization," *Magnetic Resonance Imaging*, vol. 11, pp. 873-887, 1993.
- [6] G. Castellano, L. Bonilha, L. M. Li and F. Cendes, "Texture analysis of medical images.," *Clinical Radiology*, vol. 59, pp. 1061-1069, 2004.
- [7] A. Kassner and R. E. Thornhill, "Texture analysis: A review of neurologic MR imaging applications," *American Journal of Neuroradiology*, vol. 31, p. 809–816, 2010.
- [8] H. Johansen and T. E. B. Berg, *Diffusion MRI: From Quantitative Measurement to In vivo Neuroanatomy*, San Diego, USA: Academic Press, 2009.
- [9] G. Liney, *MRI from A to Z: A Definitive Guide for Medical Professionals*, Springer Science & Business Media, 2010.

- [10] A. B. Wolbarst, *Looking Within: How X-ray, CT, MRI, Ultrasound, and Other Medical Images are Created, and how They Help Physicians Save Lives*, University of California Press, 1999.
- [11] J. T. Bushberg and J. M. Boone, *The Essential Physics of Medical Imaging*, Lippincott Williams & Wilkins, 2011.
- [12] F. Wehrli, J. MacFall, G. Glover and N. Grigsby, "The dependence of Nuclear Magnetic Resonance (NMR) image contrast on intrinsic and pulse sequence timing parameters," *Magnetic Resonance Imaging*, vol. 2, no. 1, pp. 3-16, 1984.
- [13] A. Padhani, "Dynamic contrast-enhanced MRI in clinical oncology: Current status and future directions.," *Journal of Magnetic Resonance Imaging*, vol. 16, no. 4, pp. 407-422, 2002.
- [14] Q. Li and R. M. Nishikawa, *Computer-Aided Detection and Diagnosis in Medical Imaging*, New York: Taylor & Francis, 2015 .
- [15] S. EO and T. JE, "Spin diffusion measurements: spin-echo in the presence of a time dependent field gradient," *The Journal of Chemical Physics*, vol. 42, pp. 288-292, 1965.
- [16] P. Hagmann, L. Jonasson, P. Maeder, J.-P. Thiran, V. J. Wedeen and R. Meuli, "Understanding Diffusion MR Imaging Techniques: From Scalar Diffusion-weighted Imaging to Diffusion Tensor Imaging and Beyond," *RadioGraphics*, vol. 26, pp. 205-223, 2006.
- [17] D. L. Bihan, E. Breton, L. D, A. ML, V. J and L.-J. M, "Separation of diffusion and perfusion in intravoxel incoherent motion MR imaging," *Radiology*, vol. 168, no. 2, pp. 497-505, 1988.
- [18] C. Loizou, S. Petroudi, I. Seimenis, M. Pantziaris and C. Pattichis, "Quantitative texture analysis of brain white matter lesions derived from T2-weighted MR images in MS patients with clinically isolated syndrome.," *Journal of Neuroradiology*, vol. 42, no. 2, pp. 99-114, 2015.
- [19] X. Chen, X. Wei, Z. Zhang, R. Yang, Y. Zhu and X. Jiang, "Differentiation of true-progression from pseudoprogression in glioblastoma treated with radiation therapy and concomitant temozolomide by GLCM texture analysis of conventional MRI," *Clinical Imaging*, 2015.
- [20] P. Brynolfsson, D. Nilsson, R. Henriksson, J. Hauksson, M. Karlsson, A. Garpebring, R. Birgander, J. Trygg, T. Nyholm and T. Asklund, "ADC texture—An imaging biomarker for high-grade glioma?," *Medical Physics*, vol. 41, no. 10, 2014.

- [21] Q. Ain, .ArfanJaffar and Tae-SunChoic, "Fuzzy anisotropic diffusion based segmentation and texture based ensemble classification of brain tumor.," *Applied SoftComputing*, vol. 21, pp. 330-340, 2014.
- [22] P. A. Freeborough and N. C. Fox, "MR Image Texture Analysis Applied to the Diagnosis and Tracking of Alzheimer's Disease," *IEEE TRANSACTIONS ON MEDICAL IMAGING*,, vol. 17, no. 3, pp. 475-479, 1998.
- [23] M. S. d. Oliveira, L. E. Betting, S. B. Mory, F. Cendes and G. Castellano, "Texture analysis of magnetic resonance images of patients with juvenile myoclonic epilepsy.," *Epilepsy & Behavior*, vol. 27, pp. 22-28, 2013.
- [24] N. Ghosh, Y. Sun, B. Bhanu, S. Ashwal and A. Obenaus, "Automated detection of brain abnormalities in neonatal hypoxia ischemic injury from MR images," *Medical Image Analysis*, vol. 18, pp. 1059-1069, 2014.
- [25] J. Hugosson, S. Carlsson, G. Aus, S. Bergdahl, A. Khatami, P. Loddning, C.-G. Pihl, J. Stranne, E. Holmberg and H. Lilja, "Mortality results from the Göteborg randomised population-based prostate-cancer screening trial.," *Lancet Oncology*, vol. 11, pp. 752-753, 2010.
- [26] N. D. E, "PSA testing for prostate cancer improves survival—but can we do better?," *The Lancet Oncology*, vol. 11, no. 8, pp. 702-703, 2010.
- [27] N. B. Delongchamps, M. Peyromaure, A. Schull, F. Beuvon, N. Bouazza, T. Flam, M. Zerbib, N. Muradyan, P. Legman and F. Cornud, "Prebiopsy Magnetic Resonance Imaging and Prostate Cancer Detection: Comparison of Random and Targeted Biopsies," *THE JOURNAL OF UROLOGY*, vol. 189, pp. 493-499, 2013.
- [28] Y. Peng, Y. Jiang, T. Antic, M. L. Giger, S. E. Eggener and A. Oto, "Validation of Quantitative Analysis of Multiparametric Prostate MR Images for Prostate Cancer Detection and Aggressiveness Assessment: A Cross-Imager Study.," *Radiology*, vol. 271, no. 2, pp. 461-471, 2014.
- [29] S. I. Jung, O. F. Donati, H. A. Vargas, D. Goldman, H. Hricak and O. Akin, "Transition Zone Prostate Cancer: Incremental Value of Diffusion-weighted Endorectal MR Imaging in Tumor Detection and Assessment of Aggressiveness.," *Radiology*, vol. 269, no. 2, pp. 493-503, 2013.
- [30] A. Vignati, S. Mazzetti, V. Giannini¹, F. Russo, E. Bollito, F. Porpiglia, M. Stasi and D. Regge, "Texture features on T2-weighted magnetic resonance imaging: new potential biomarkers for prostate cancer aggressiveness.," *Physics in Medicine & Biology*, vol. 60, pp. 2685-2701, 2015.
- [31] E. Niaf, O. Rouviere, F. Mege-Lechevallier, F. Bratan and C. Lartizien, "Computer-aided

diagnosis of prostate cancer in the peripheral zone using multiparametric MRI," *Physics in medicine and biology*, vol. 57, pp. 3833-3851, 2012.

- [32] A. Madabhushi, M. D. Feldman, D. N. Metaxas, J. Tomaszewski and D. Chute, "Automated Detection of Prostatic Adenocarcinoma From High-Resolution Ex Vivo MRI," *IEEE TRANSACTIONS ON MEDICAL IMAGING*, vol. 24, no. 12, pp. 1611-1625, 2005.
- [33] P. Debbie Saslow, M. P. Carla Boetes, M. P. Wylie Burke, M. Steven Harms, P. Martin O. Leach, M. P. Constance D. Lehman, M. Elizabeth Morris, M. Etta Pisano, M. P. Mitchell Schnall, M. Stephen Sener, P. Robert A. Smith and M. Ellen Warner, "American Cancer Society Guidelines for Breast Screening with MRI as an Adjunct to Mammography.," *American Cancer Journal for Clinicians*, vol. 57, no. 2, pp. 75-89, 2007.
- [34] K. Nie, J.-H. Chen, H. J. Yu, Y. Chu, O. Nalcioğlu and M.-Y. Su, "Quantitative Analysis of Lesion Morphology and Texture Features for Diagnostic Prediction in Breast MRI," *Academic Radiology*, vol. 15, no. 2, pp. 1513-1525, 2008.
- [35] W. Chen, M. L. Giger, H. Li, U. Bick and G. M. Newstead, "Volumetric Texture Analysis of Breast Lesions on Contrast-Enhanced Magnetic Resonance Images," *Magnetic Resonance in Medicine*, vol. 58, pp. 562-571, 2007 .
- [36] B. J. Woods, B. D. Clymer, T. Kurc, J. T. Heverhagen, R. Stevens, A. Orsdemir, O. Bulan and M. V. K. MD, "Malignant-lesion segmentation using 4D co-occurrence texture analysis applied to dynamic contrast-enhanced magnetic resonance breast image data," *Journal of Magnetic Resonance Imaging*, vol. 25, no. 3, pp. 495-501, 2007.
- [37] J. Yao, J. Chen and C. Chow, "Breast Tumor Analysis in Dynamic Contrast Enhanced MRI Using Texture Features and Wavelet Transform," *Selected Topics in Signal Processing*, vol. 3, no. 1, pp. 94-100, 2009.
- [38] M. Kriege, C. T. Brekelmans, C. Boetes, P. E. Besnard, H. M. Zonderland, I. M. Obdeijn, R. A. Manoliu, T. Kok, H. Peterse, M. M. Tilanus-Linthorst, S. H. Muller, S. Meijer, J. C. Oosterwijk, L. V. Beex and R. A.E.M, "Efficacy of MRI and Mammography for Breast-Cancer Screening in Women with a Familial or Genetic Predisposition," *The new England journal of medicine*, vol. 351, no. 5, pp. 427-437, 2004.
- [39] C. D. Lehman, C. Gatsonis, C. K. Kuhl, R. E. Hendrick, E. D. Pisano, L. Hanna, S. Peacock, S. F. Smazal, D. D. Maki, T. B. Julian, E. R. DePeri, D. A. Bluemke and M. D. Schnall, "MRI Evaluation of the Contralateral Breast in Women with Recently Diagnosed Breast Cancer," *The new england journal of medicine*, vol. 356, no. 13, pp. 1295-303, 2007.
- [40] F. Sardanelli, G. M. Giuseppetti, P. Panizza, M. Bazzocchi, A. Fausto, G. Simonetti, V. Lattanzio and A. D. Maschio, "Sensitivity of MRI Versus Mammography for Detecting Foci of Multifocal, Multicentric Breast Cancer in Fatty and Dense Breasts Using the Whole-

Breast Pathologic Examination as a Gold Standard," *American journal of radiology*, vol. 183, p. 1149–1157, 2004.

- [41] M. D. SCHNALL, J. BLUME, D. A. BLUEMKE, G. A. DEANGELIS, N. DEBRUHL, S. HARMS, S. H. H.-K. BRUNNER, N. HYLTON, C. K. KUHLE, E. D. PISANO, P. CAUSER, S. J. SCHNITT, S. F. SMAZAL, C. B. STELLING and CONSTAN, "MRI Detection of Distinct Incidental Cancer in Women With Primary Breast Cancer Studied in IBMC 6883".
- [42] Ö. Özsarlak, P. M. Parizel, A. M. D. Schepper, P. D. Jonghe and J. J. Martin, "Whole-body MR screening of muscles in the evaluation of neuromuscular diseases.," *EUROPEAN RADIOLOGY*, vol. 14, p. 1489–1493, 2004.
- [43] M. Jarraya, S. Quijano-Roy, N. Monnier, A. Be'hin, D. Avila-Smirnov, N. B. Romero, V. Allamand, P. Richard, A. Barois, A. May, B. Estournet, E. Mercuri, P. G. Carlier and R.-Y. Carlier, "Whole-Body muscle MRI in a series of patients with congenital myopathy related to TPM2 gene mutations.," *Neuromuscular Disorders*, vol. 22, pp. 137-147, 2012.
- [44] S. Quijano-Roy, D. Avila-Smirnow and R. Y. Carlier, "Whole body muscle MRI protocol: Pattern recognition in early onset NM disorders.," *Neuromuscular Disorders*, vol. 22, pp. 68-84, 2012.
- [45] V. Straub, P. G. Carlier and E. Mercuri, "TREAT-NMD workshop: Pattern recognition in genetic muscle diseases using muscle MRI," *Neuromuscular Disorders*, vol. 22, pp. 42-53, 2012.
- [46] E. Amarteifio, A. M. Nagel, H.-U. Kauczor and M.-A. Weber, "Functional imaging in muscular diseases.," *Insights Imaging*, vol. 2, p. 609–619, 2011.
- [47] M. J. O'Connell, T. Powell, D. Brennan, T. Lynch, C. J. McCarthy and S. J. Eustace, "Whole-Body MR Imaging in the Diagnosis of Polymyositis.," *American journal of radiology*, vol. 179, p. 967–971, 2002.
- [48] S. Herlidou, Y. Rolland, J. Y. Bansard, E. L. Rumeur and J. D. d. Certaines, "Comparison of automated and visual texture analysis in MRI: Characterization of normal and diseased skeletal muscle," *Magnetic Resonance Imaging*, vol. 17, no. 9, pp. 1393-1397, 1999.
- [49] J. Phoenix, D. Betal, N. Roberts, T. R. Helliwell and R. H. Edwards, "Objective quantification of muscle and fat in human dystrophic muscle by magnetic resonance image analysis," *Muscle & Nerve*, vol. 19, no. 3, pp. 302-310, 1996.
- [50] D. M. Ghoneim, Y. Cherelb, L. Lemairec, J. D. d. Certaines and A. Maniere, "Texture analysis of magnetic resonance images of rat muscles during atrophy and regeneration," *Magnetic Resonance Imaging*, vol. 24, no. 2, pp. 167-171, 2006.

- [51] T. K. Chuah, E. V. Reeth, K. Sheah and C. L. Poh, "Texture analysis of bone marrow in knee MRI for classification of subjects with bone marrow lesion — Data from the Osteoarthritis Initiative.," *Magnetic Resonance Imaging*, vol. 31, pp. 930-938, 2013.
- [52] N. Ghanem, C. Lohrmann, M. Engelhardt, G. Pache, M. Uhl, U. Saueressig, E. Kotter and M. Langer, "Whole-body MRI in the detection of bone marrow infiltration in patients with plasma cell neoplasms in comparison to the radiological skeletal survey," *European Radiology*, vol. 16, no. 5, p. 1005–1014, 2006.
- [53] H. J. Adams, T. C. Kwee, H. M. Lokhorst, P. E. Westerweel, R. Fijnheer, a. J. Kersten, H. M. Verkooijen, J. Stoker and R. A. Nievelstein, "Potential Prognostic Implications of Whole-Body Bone Marrow MRI in Diffuse Large B-Cell Lymphoma Patients With a Negative Blind Bone Marrow Biopsy.," *JOURNAL OF MAGNETIC RESONANCE IMAGING*, vol. 39, p. 1394–1400, 2014.
- [54] J. Wight, E. Morris, A. Stillwell, B. Grant, H. C. Lai and I. Irving, "Screening whole spine Magnetic Resonance Imaging (MRI) in multiple myeloma1," *Internal medicine journal*, vol. 45, no. 7, pp. 762-765, 2015.
- [55] Hofmann, K. J, B. M, P. M and A. N, "Bone marrow edema in the knee. Differential diagnosis and therapeutic possibilities.," *Der Orthopade*, vol. 35, no. 4, pp. 476-477, 2006.
- [56] S. L. Giles, N. M. deSouza, D. J. Collins, V. A. Morgan, S. West, F. E. Davies, G. J. Morgan and C. Messiou, "Assessing myeloma bone disease with whole-body diffusion-weighted imaging: comparison with x-ray skeletal survey by region and relationship with laboratory estimates of disease burden.," *Clinical Radiology*, vol. 70, pp. 614-621, 2015.
- [57] K. Klodowski, J. Kaminski, K. Nowickab, J. Tarasiuka, S. Wronski, M. Swietek, M. Blazewicz, H. Figiel, K. Turek and T. Szponder, "Micro-imaging of implanted scaffolds using combined MRI and micro-CT," *Computerized Medical Imaging and Graphics*, vol. 38, p. 458–468, 2014.
- [58] K. E, F. G, D. M. A, B. M, M. A, P. F and M. M, "Clinical Results and MRI Evolution of a Nano-Composite Multilayered Biomaterial for Osteochondral Regeneration at 5 Years," *The American Journal of Sports Medicine*, vol. 42, no. 1, pp. 158-165, 2013.
- [59] S. Majumdar, H. K. Genant, S. Grampp, M. D. Jergas, D. C. Newitt and A. A. Gies, "Analysis of trabecular bone structure in the distal radius using high-resolution MRI," *European Radiology*, vol. 4, pp. 517-524, 1994.
- [60] T. M. LINK, S. MAJUMDAR, J. C. LIN, D. NEWITT and P. AUGAT, "A Comparative Study of Trabecular Bone Properties in the Spine and Femur Using High Resolution MRI and CT," *JOURNAL OF BONE AND MINERAL RESEARCH*, vol. 13, no. 1, pp. 122-132, 1998.

- [61] V. VIETH, T. M. LINK, A. LOTTER, T. PERSIGEHL and D. NEWITT, "Does the Trabecular Bone Structure Depicted by High-Resolution MRI of the Calcaneus Reflect the True Bone Structure?," *Investigative Radiology*, vol. 36, no. 4, pp. 210-217, 2001.
- [62] L. C. Harrison, R. Nikander, M. Sikio, T. Luukkaala, M. T. Helminen, P. Ryymin, S. Soimakallio, H. J. Eskola, P. Dastidar and H. Sieva, "MRI Texture Analysis of Femoral Neck: Detection of Exercise Load-Associated Differences in Trabecular Bone," *JOURNAL OF MAGNETIC RESONANCE IMAGING*, vol. 34, pp. 1359-1366, 2011.
- [63] C. M, S. E, S. F, M. G, G. S, S. G and P.-M. R, "Diffusion-weighted MRI in the evaluation of renal lesions: preliminary results.," *The british journal of radiology*, vol. 77, no. 922, pp. 851-857, 2004.
- [64] J. J. Nikken and G. P. Krestin, "MRI of the kidney—state of the art," *European Radiology*, vol. 17, p. 2780–2793, 2007.
- [65] M. Hashemieh, A. Azarkeivan, S. Akhlaghpour, A. Shirkavand and K. Sheibani, "T2-star (T2*) Magnetic Resonance Imaging for Assessment of Kidney Iron Overload in Thalassaemic Patients.," *Archives of Iranian Medicine*, vol. 15, no. 2, pp. 91-94, 2012.
- [66] N. Michoux, J.-P. Vallée, A. Pechère-Bertschi, X. Montet, L. Buehler and B. E. V. Beers, "Analysis of contrast-enhanced MR images to assess renal function.," *Magnetic Resonance Materials in Physics, Biology and Medicine*, vol. 19, no. 4, pp. 167-179, 2006.
- [67] F. G. Zöllner, R. Sance, P. Rogelj, M. J. Ledesma-Carbayo, J. Rørvik, A. Santos and A. Lundervold, "Assessment of 3D DCE-MRI of the kidneys using non-rigid image registration and segmentation of voxel time courses," *Computerized Medical Imaging and Graphics*, vol. 33, no. 3, pp. 171-181, 2009.
- [68] P. Gujral, A. M, B. D, V. J-p, M. X and M. N, "Classification of magnetic resonance images from rabbit renal perfusion," *Chemometrics and Intelligent Laboratory Systems*, vol. 98, no. 2, pp. 173-181, 2009.
- [69] T.-Y. Kim, N.-H. Cho, G.-B. Jeong, E. Bengtsson and H.-K. Choi, "3D Texture Analysis in Renal Cell Carcinoma Tissue Image Grading," *Computational and Mathematical Methods in Medicine*, vol. 2014, p. 12, 2014.
- [70] L. Bokacheva, HenryRusinek, J. L. Zhang and V. S. Lee, "Assessment of Renal Function with Dynamic Contrast-Enhanced MR Imaging," *Magnetic Resonance Imaging Clinics of North America*, vol. 16, no. 4, pp. 597-611, 2008.
- [71] T. Woodard, S. Sigurdsson, J. Gotal, A. Torjesen, L. Inker, T. Aspelund, G. Eiriksdottir, V. Gudnason, T. Harris, L. Launer, A. Levey and G. Mitchell, "Segmental kidney volumes measured by dynamic contrast-enhanced magnetic resonance imaging and their

- association with CKD in older people," *American Journal of Kidney Diseases*, vol. 65, no. 1, pp. 41-48, 2014.
- [72] E. Belloni, F. D. Cobelli, A. Esposito, R. Mellone, G. Perseghin, T. Canu and A. D. Maschio, "MRI of Cardiomyopathy," *American Journal of Roentgenology*, vol. 191, no. 6, pp. 1702-1710, 2008.
- [73] R. Manzke, L. Binner, A. Bornstedt, N. Merkle, A. Lutz, R. Gradingner and V. Rasche, "Assessment of the coronary venous system in heart failure patients by blood pool agent enhanced whole-heart MRI," *European Radiology*, vol. 21, no. 4, pp. 799-806, 2011.
- [74] K. LP, E. K, S. K, M. F, O. S, W. L and E. T, "Probability mapping of scarred myocardium using texture and intensity features in CMR images.," *Biomedical Engineering Online*, pp. 12-91, 2013.
- [75] S. Jamil-Copley, W. Bai, B. Ariff, P. Lim, M. Koa-Wing, A. Kyriacou, S. Hayat, A. Sohaib, N. Qureshi, B. Sandler, D. O'Regan, Z. Whinnett, W. Davies, D. Rueckert, P. Kanagaratnam and N. Peters, "LGE MRI ischaemic scar thickness gradient predicts inducible ventricular," in *Heart Rhythm Congress*, Denver, 2013.
- [76] O. Buckley, R. Madan, R. Kwong, F. J. Rybicki and A. Hunsaker, "Cardiac Masses, Part 1: Imaging Strategies and Technical Considerations," *American Journal of Roentgenology*, vol. 197, no. 5, pp. 837-841, 2011.
- [77] O. Buckley, R. Madan, R. Kwong, F. J. Rybicki and A. Hunsaker, "Cardiac Masses, Part 2: Key Imaging Features for Diagnosis and Surgical Planning," *American Journal of Roentgenology*, vol. 197, no. 5, pp. 842-851, 2011.
- [78] P. Sparrow, D. R. Messroghli, S. Reid, J. P. Ridgway, G. Bainbridge and M. U. Sivananthan, "Myocardial T1 Mapping for Detection of Left Ventricular Myocardial Fibrosis in Chronic Aortic Regurgitation: Pilot Study," *American Journal of Roentgenology*, vol. 187, no. 6, pp. 630-635, 2006.
- [79] R. R, H. DL, K. SF, M. ME, M. V, H. S, R. K, B. M, V. V. J, H. DJ and B. E, "Cardiac catheterisation guided by MRI in children and adults with congenital heart disease.," *The Lancet*, vol. 362, pp. 1877-1882, 2003.
- [80] J. V, B. EM, L. DJ, L. JM, S. PJ, N. MY, L. NA, N. SC, M. LM, Y. AG and W. FW, "Cerebral oxygen metabolism in neonates with congenital heart disease quantified by MRI and optics.," *Journal of Cerebral Blood Flow & Metabolism*, vol. 34, no. 3, p. 380–388, 2014.
- [81] P. Rajiah and J. P. Kanne, "Cardiac MRI: Part 1, Cardiovascular Shunts," *American Journal of Roentgenology*, vol. 197, no. 4, pp. 603-620, 2011.

- [82] P. Rajiah, "Cardiac MRI: Part 2, Pericardial Diseases," *American Journal of Roentgenology*, vol. 197, no. 4, pp. 621-634, 2011.
- [83] E. A. Zerhouni, D. M. Parish, W. J. Rogers, S. A. Yang and E. P. Shapiro, "Human Heart: Tagging with MR Imaging A Method for Noninvasive Assessment of Myocardial Motion," *Radiology*, vol. 169, pp. 59-63, 1988.
- [84] L. Axel and L. Dougherty, "MR imaging of motion with spatial modulation of magnetization," *Radiology*, vol. 171, pp. 841-845, 1989.
- [85] A. Histace, B. Matuszewski and Y. Zhang, "Segmentation of Myocardial Boundaries in Tagged Cardiac MRI Using Active Contours: A Gradient-Based Approach Integrating Texture Analysis," *International Journal of Biomedical Imaging*, vol. 2009, p. 8 pages, 2009.
- [86] W. S. Kerwin, N. F. Osman and J. L. Prince, "Image Processing and Analysis in Tagged Cardiac MRI," in *I. Bankman, Ed., Handbook of Medical Imaging: Processing and Analysis*, 2000.
- [87] T. F. Budinger, A. Berson, E. R. McVeigh, R. I. Pettigrew, G. M. Pohost, J. T. Watson and S. A. Wickline, "Cardiac MR imaging: report of a working group sponsored by the National Heart, Lung, and Blood Institute.," *Radiology*, vol. 208, no. 3, pp. 573-576, 1998.
- [88] N. F. Osman, W. S. Kerwin, E. R. McVeigh and J. L. Prince, "Cardiac motion tracking using CINE harmonic phase (HARP) magnetic resonance imaging," *Magnetic Resonance in Medicine*, vol. 42, no. 6, pp. 1048-1060, 1999.
- [89] N. Osman, E. McVeigh and J. Prince, "Imaging heart motion using harmonic phase MRI," *Medical Imaging, IEEE Transactions*, vol. 19, no. 3, pp. 186-202, 2000.
- [90] M. P, S. TS, T. SV, M. A, S.-J. H and P. EM, "Two-phase active contour method for semiautomatic segmentation of the heart and blood vessels from MRI images for 3D visualization.," *Computerized Medical Imaging and Graphics*, vol. 26, no. 1, pp. 9-17, 2003.
- [91] H. Zhang, A. Wahle, R. Johnson and T. Scholz, "4-D Cardiac MR Image Analysis: Left and Right Ventricular Morphology and Function," *Medical Imaging, IEEE Transactions*, vol. 29, no. 2, pp. 350-364, 2010.
- [92] T. Glatard, J. Montagnat and I. E. Magnin, "Texture based medical image indexing and retrieval: application to cardiac imaging," in *Proceedings of the 6th ACM SIGMM international workshop on Multimedia information retrieval*, New York, USA, 2004.
- [93] V. S, R. A, P. SR, G. K, L. CG, M. V, A. G, B. RB and S. K, "Urinary bladder cancer: role of

MR imaging," *Radiographics*, vol. 32, no. 2, pp. 371-387, 2012 .

- [94] T. A, K. I, I. K, S. G, S. M, N. K, T. R and B. D, "Dynamic MRI of bladder cancer: evaluation of staging accuracy.," *American Journal of Roentgenology*, vol. 184, no. 1, pp. 121-127, 2005.
- [95] K. O, C. T, I. E, K. A, B. S, T. N and G. N, "Diffusion-weighted MRI of urinary bladder and prostate cancers.," *Diagnostic and interventional Radiology*, vol. 15, no. 2, pp. 104-110, 2009.
- [96] A. S, K. MN, C. K, B. MD and U. O, "The value of diffusion-weighted MRI in the diagnosis of malignant and benign urinary bladder lesions.," *The British Journal of Radiology*, vol. 84, no. 1006, pp. 875-882, 2011.
- [97] W. H, K. M, K. H, G. S, T. Y, O. M and M. N, "Preoperative T staging of urinary bladder cancer: does diffusion-weighted MRI have supplementary value?," *American Journal of Roentgenology*, vol. 192, no. 5, pp. 1361-1366, 2009.
- [98] N. Tuncbilek, M. Kaplan, S. Altaner, I. H. Atakan, N. Süt, O. Inci and M. K. Demir, "Value of Dynamic Contrast-Enhanced MRI and Correlation with Tumor Angiogenesis in Bladder Cancer," *American Journal of Roentgenology*, vol. 192, no. 4, pp. 949-955, 2009.
- [99] S. Z, Y. Z, Z. G, C. G, X. X, L. Z and L. H, "Characterization of texture features of bladder carcinoma and the bladder wall on MRI: initial experience.," *Academic Radiology*, vol. 20, no. 8, pp. 930-938, 2013.
- [100] Z. Shi, J. Yang, G. Zhang and H. Lu, "Characterization of Texture Features Between Carcinomatous and Normal Wall Tissue in MR Bladder Imaging," in *Biomedical Engineering and Informatics, 2009. BMEI '09. 2nd International Conference*, Tianjin, 2009.
- [101] K. AD, A. AT, T. EW, T. GM and M. C, "Staging papillary carcinoma of the thyroid: magnetic resonance imaging vs ultrasound of the neck.," *Clinical Radiology*, vol. 55, no. 3, pp. 222-226, 2000.
- [102] J. K. Hoang, W. K. Lee, M. Lee, D. Johnson and S. Farrell, "US Features of Thyroid Malignancy: Pearls and Pitfalls," *RadioGraphics*, vol. 27, no. 3, p. 847–860, 2007.
- [103] H. JK, B. B. 4th, G. AR, L. WK and G. CM, "Imaging of thyroid carcinoma with CT and MRI approaches to common scenarios," *Cancer Imaging*, vol. 13, pp. 128-139, 2013.
- [104] K. JE, "Computed tomography and magnetic resonance imaging in diseases of the thyroid and parathyroid.," *European Journal of Radiology*, vol. 66, no. 3, pp. 480-492, 2008.

- [105] D. M, L. JT, W. T, M. TW, C. SP, B. NT, B. P, B. G, C. H, M. JR and D. JC, "MRI texture analysis predicts p53 status in head and neck squamous cell carcinoma.," *American Journal of Radiology*, vol. 36, no. 1, pp. 166-170, 2015.
- [106] N. Albiin, "MRI of Focal Liver Lesions," *Current Medical Imaging Reviews*, vol. 8, no. 2, p. 107–116, 2012 .
- [107] A. A, K. DM, C. DJ, B. M, W. T, L. MO and O. MR, "Measurement reproducibility of perfusion fraction and pseudodiffusion coefficient derived by intravoxel incoherent motion diffusion-weighted MR imaging in normal liver and metastases.," *European Radiology*, vol. 23, no. 2, pp. 428-434, 2013 .
- [108] B. M and R. EJ, "Hepatic metastases: use of diffusion-weighted echo-planar imaging.," *Abdominal Imaging*, vol. 35, no. 4, pp. 454-461, 2010 .
- [109] L. M, F. L, V. A, A. L, M. Y and R. O, "The diffusion-weighted imaging perfusion fraction f is a potential marker of sorafenib treatment in advanced hepatocellular carcinoma: a pilot study.," *European Radiology*, vol. 21, no. 2, pp. 281-290, 2011.
- [110] P.-X. Lu, H. Huang, J. Yuan, F. Zhao, Z.-Y. Chen, Q. Zhang, A. T. Ahuja, B.-P. Zhou and Y.-X. J. Wáng, "Decreases in Molecular Diffusion, Perfusion Fraction and Perfusion-Related Diffusion in Fibrotic Livers: A Prospective Clinical Intravoxel Incoherent Motion MR Imaging Study," 1 December 2014. [Online]. Available: <http://www.ncbi.nlm.nih.gov/pmc/articles/PMC4250077/pdf/pone.0113846.pdf>. [Accessed 23 5 2015].
- [111] J. D, D. M and H. M. Taimr P, "Texture analysis of human liver.," *J Magn Reson Imaging.*, vol. 15, no. 1, pp. 68-74, 2002.
- [112] D. Mahmoud-Ghoneim, A. Amin and P. Corr, "MRI-based texture analysis: a potential technique to assess protectors against induced-liver fibrosis in rats.," *Radiol Oncol*, vol. 43, no. 1, pp. 30-40, 2009.
- [113] K. H, K. M, Z. X, S. M, K. H, G. S and F. H, "Computer-aided diagnosis of hepatic fibrosis: preliminary evaluation of MRI texture analysis using the finite difference method and an artificial neural network.," *AJR Am J Roentgenol*, vol. 189, no. 1, pp. 117-122, 2007.
- [114] C. Güngör, B. T. Hofmann, G. Wolters-Eisfeld and M. Bockhorn, "Pancreatic cancer Review," *The British Pharmacological Society*, vol. 171, pp. 849-858, 2014.
- [115] E. S. Lee and J. M. Lee, "Imaging diagnosis of pancreatic cancer: A state-of-the-art review," *World Journal of Gastroenterology*, vol. 20, no. 24, pp. 7864-7877, 2014.
- [116] R. S. P, H. K. M and F. E. K, "Multimodality imaging of pancreatic cancer-computed tomography, magnetic resonance imaging, and positron emission tomography.," *Cancer*

journal, vol. 18, no. 6, pp. 511-522, 2012.

- [117] K. Sandrasegaran, C. Lin, F. M. Akisik and M. Tann, "State-of-the-Art Pancreatic MRI," *American Roentgen Ray Society*, vol. 195, pp. 42-53, 2010.
- [118] D.-C. He and L. Wang, "Texture Unit, Texture Spectrum, And Texture Analysis," *Geoscience and Remote Sensing, IEEE Transactions*, vol. 28, no. 4, pp. 509-512, 1990.
- [119] N. Aggarwal and R. K. Agrawal, "First and Second Order Statistics Features for Classification of Magnetic Resonance Brain Images," *Journal of Signal and Information Processing*, vol. 3, pp. 146-153, 2012.
- [120] L. Sharan, C. Liu, R. Rosenholtz and E. H. Adelson, "Recognizing Materials using Perceptually Inspired Features," *international journal of computer vision*, vol. 103, no. 3, pp. 348-371, 2013.
- [121] Duda and Dorota, "Texture analysis as a tool for medical decision support. Part 1 recent applications for cancer early detection," *Advances in Computer Science Research*, vol. 11, pp. 61-84, 2014.
- [122] E. H. Linfoot, "An Informational Measure of Correlation," *Information and Control*, vol. 1, no. 1, pp. 85-89, 1957.
- [123] C. B. Bell, "Mutual Information and Maximal Correlation as Measures of Dependence," *The Annals of Mathematical Statistics*, vol. 33, no. 2, pp. 587-595, 1962.
- [124] J. S. Weszka, C. R. Dyer and A. Rosenfeld, "Comparative Study Texture Measures Terrain Classification," *IEEE TRANSACTIONS ON SYSTEMS, MAN, AND CYBERNETICS*, Vols. SMC-6, no. 4, pp. 269-285, 1976.
- [125] M.-H. Horng, Y.-N. Sum and X.-Z. Lin, "Texture feature coding method for classification of liver sonography.," *Computerized Medical Imaging and Graphics*, vol. 26, pp. 33-42, 2002.
- [126] A. P. Pentland, "Shading into texture," in *Proceedings of the Fourth National Conference on Artificial Intelligence*, Austin, Texas, 1984.
- [127] N. Sarkar and B. Chaudhuri, "An efficient differential box-counting approach to compute fractal dimension of image," *Systems, Man and Cybernetics, IEEE Transactions on*, vol. 24, no. 1, pp. 115-120, 1994.
- [128] C. B. B and N. Sarkar, "Texture Segmentation Using Fractal Dimension," *IEEE TRANSACTIONS ON PATTERN ANALYSIS AND MACHINE INTELLIGENCE*, vol. 17, no. 1, pp. 72-77, 1995.

- [129] W. Kruskal and W. Allen, "Use of Ranks in One-Criterion Variance Analysis," vol. 47, pp. 583-621, 1952.
- [130] J. A. Nelder and R. W. M. Wedderburn, "Generalized Linear Models," *Journal of the Royal Statistical Society*, vol. 135, no. 3, 1972.
- [131] Y. Freund and R. E. Schapire, "A Decision-Theoretic Generalization of on-Line Learning and an Application to Boosting," 1997.
- [132] A. Khademi, S. Krishnan and A. Venetsanopoulos, "Shift-Invariant DWT for Medical Image Classification," 2011.
- [133] W. H. Nailon, "Texture Analysis Methods for Medical Image Characterisation," 2010.